

Supplementary Material

S1. Model mechanisms related to the formation and removal of particulate matter

S1.1 Gas and aerosol modules

The formation rates of gases are controlled by the gas modules in the models. And the gas-aerosol equilibrium in aerosol module determines the conversion to aerosol phases. The gas modules include Statewide Air Pollution Research Center (SAPRC99), Regional Atmospheric Deposition Model (RADM), Regional Atmospheric Chemistry Mechanism (RACM) and Carbon-Bond Mechanism version Z (CBMZ). Following are brief descriptions of these modules:

- (1) SAPRC-99: This mechanism is developed for the gas-phase atmospheric reactions of NO_x and VOCs in the urban and regional atmospheres (Carter, 2000). It contains reactions for about 400 types of VOCs with about 500 VOCs categories, aiming for the explicit representation of VOCs in atmospheric reactions. The modeled O_3 concentration is higher than its updated version SAPRC07, owing to higher OH formation rates in the related reactions (Li et al., 2012; Shearer et al., 2012).
- (2) RADM2 and RACM: The version 2 of RADM module is a gas-phase chemistry mechanism developed originally for use in the Regional Acid Deposition Model. The module has altogether 63 species, including 21 inorganic species and 42 organic species. The species and reactions included in the module are listed in (Stockwell et al., 1990). The RACM module is an update version of RADM with more biogenic VOCs included and more coupling options. The number of organic species increased from 42 to 56, and the overall reaction increases from 220 to 237. The species and reactions are documented in (Stockwell et al., 1997).
- (3) CBMZ: This module is updated from the Carbon Bond Mechanism (CBM-IV) (Zaveri and Peters, 1999). It includes 67 species and 164 reactions. The lumped structure is used to group large numbers of organic compounds into several sets of VOCs categories according to their similarity in oxidation reactivity and emission magnitudes.

Figure S1 compares the reaction rates of the main reactions of producing SO_4^{2-} and NO_3^- by different mechanisms adopted by models in this study. The dominating reaction to form SO_4^{2-} is reaction with the OH radical. The simplified reaction is shown in reaction S1. According to fig. S1, the formation rates are consistent among different mechanisms except that RADM2 has lower reaction rate than others. In case of NO_3^- , the principle formation path for HNO_3 in the daytime is reaction S2. Another 3 reactions in the models are shown in reactions S3-S5. According to fig. S1, the reaction (2) has the highest reaction rate among all reactions for gas-phase production of HNO_3 . The SAPRC-99, BC05 and RACM2 have similar reaction rates, while RADM2 and CBMZ have lower values. Another important reaction is (3) $\text{NO}_3 + \text{HO}_2$. The SAPRC-99 mechanism has slightly higher reaction rate than the others, while RACM is the lowest one and the rate about 2/3 of SAPRC99.





At night-time, NO reacts rapidly with O₃ to form NO₂ (reaction S6), and eventually forms N₂O₅ through reactions S7-8. The N₂O₅ gas can react with H₂O (liquid) to form HNO₃, which is called the heterogeneous reaction of N₂O₅ (as shown in reaction S9). This is another main pathway to convert gas phase NO_x to particle phase HNO₃. N₂O₅ can also react with vapour phase of H₂O (gas-phase reaction), but the reaction rate is not compatible with the heterogeneous reaction. The CB05 module includes additional reaction S10.

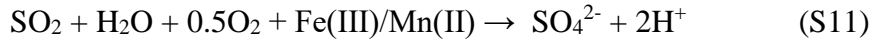


This formation of nitrate is sensitive to parameterization of the heterogeneous reaction related to NO₂, HONO, HNO₃ and N₂O₅ (Sartelet et al., 2008). (Zheng et al., 2015) found that model underestimate the concentration of PM_{2.5} and its components with current model mechanism by about 40-60%. After he added 9 heterogeneous reactions into the model, the model performance on SO₄²⁻ and NO₃⁻ were significantly improved from -54% to 6%. The improvements were most significant at high pollution episodes. According to fig. S1, the reaction rate of reaction S9 N₂O₅ + H₂O largely outweighs that of reaction S10 NO₂+H₂O. The reaction rates of RACM and RADM2 mechanisms are more than 5 folds quicker than the others.

The aerosol modules use in this study include AERO5/6 with ISORROPIA, Modal Aerosol Dynamics for Europe (MADE) coupled with SOA scheme based on the Volatility Basis Set (VBS) approach (SOA_VBS), and Goddard Chemistry Aerosol Radiation & Transport Model (GOCART). Following are brief descriptions of these modules:

- (1) AERO5/6 with ISORROPIA. The aerosols are divided into three modes: Aitken, accumulation and coarse modes. The gas-aerosol equilibrium is calculated by the ISORROPIA model. It predicts the partition of the composition of inorganic aerosols (Nenes et al., 1998, 1999). The first version of ISORROPIA (v1) is used in CMAQ model version before 5.0, after which the second version (v2) came out. A main change in v2 is the introduction of thermodynamics of crustal species such as Ca²⁺, K⁺ and Mg²⁺ (Fountoukis and Nenes, 2007). The corresponding impacts mainly show up on the gas-particle partitioning of NO₃⁻ and NH₄⁺ in areas with high dust emission. Also v1 presents K⁺, Ca²⁺ and Mg²⁺ as Na⁺ equivalents, and v2 treats these species separately in the model, which is also supposed to help improving the model accuracy on PM in high dust regions. Starting from v5.0, the CMAQ model also incorporates the windblown dust module and updates the speciation of PM components (Foroutan et al., 2017). Study reported that the updated treatment of crustal species in ISORROPIA v2 would reduce fine mode of PM over polluted area (Wang et al., 2012a). However, all CMAQ models turn

this option off in this study, so all WRF-CMAQ models don't consider dust emission. In addition, CMAQv471 has been reported with over-prediction of unappreciated PM_{2.5} referred as PM_{other} in the model. CMAQv502 tried to solve this problem by adopting a new speciation scheme and dividing the PM_{other} into primary NH₄⁺, Na⁺, Cl⁻, trace metals (including Mn and Fe) and non-carbon organic mass (NCOM). Beside this, CMAQv502 updated the production of SO₄²⁻ in the aqueous reaction (Appel et al., 2013). This explicit treatment of Fe and Mn allows more consistent treatment of aqueous reaction from SO₂ to SO₄²⁻ as shown in reaction S11:



- (2) MADE/SOA_VBS: The MADE is developed for detailed treatment of aerosols for mesoscale models. It also uses three modes (Aitken, accumulation and coarse modes) to present the distribution of particles, each with a lognormal distribution (Ackermann et al., 1998). The SOA_VBS is developed according to the organic aerosol partition theory (Murphy and Pandis, 2009). The partitioning of gas-particle phase for SOA species is estimated by vapor-liquid equilibrium theory, determined by effective saturation concentration of species (Murphy and Pandis, 2009).
- (3) GOCCART: This module processes emissions of S, dust, BC, OC and sea-salt. The details about the model is described in (Chin et al., 2002). These species/emissions are treated with specific modules in the model. The modeled PM is composed by SO₄²⁻, OC and BC, but no NO₃⁻ and NH₄⁺. The particle species are assumed with lognormal size distribution. SO₄²⁻ is formed from the oxidation of SO₂. BC and OC mainly come from biomass burning based on satellite observation. SO₄²⁻, BC and OC are considered as submicron aerosols with maximum radius of 0.5 μm. The sea-salt emission is generated with a function of wind speed and particle radius and is grouped into four size bins with radius (0.1-0.5, 0.5-1.5, 1.5-5 and 5-10 μm). Dust emission is calculated with probability-source function and is grouped into 7 size bins with radius (0.1-0.18, 0.18-0.3, 0.3-0.6, 0.6-1, 1-1.8, 1.8-3 and 3-6 μm).

S1.2 Dust and sea-salt emissions

Dust particles are produced when winds blow on arid and semiarid grounds. The average lifetime of dust particles is about 2-7 days in the atmosphere, which allows them to travel thousands of kilometers (Shao et al., 2011). In EA, the particles from floating dust from the Takalmakan Desert and Gobi Desert in north-western China can transport a long distance over the northern China and even reach the Pacific Ocean (Huang et al., 2008; Iwasaka et al., 2003; Liu et al., 2003; Wang et al., 2018). The estimated global dust emissions by different studies vary from 500 to 3000 Mt yr⁻¹, and ranges 170-500 Mt yr⁻¹ in Asia (Shao et al., 2011). Except the natural sources of dust, human activities can also contribute to dust emission, such as land dust caused by vehicles and construction. The contribution of anthropogenic sources on total dust emission varies largely from 10-60% (Webb and Pierre, 2018).

The amount of dust emission is uncertain owing to the uncertainty in the process of raising dust into the atmosphere. The current models employ parameterization methods to estimate the floating dust as response to wind. The dust flux can be formed by both the uplifting force of wind and saltation bombardment when particles hit the surface ground (Foroutan et al., 2017). Several

different dust schemes have been established, with differences in the ways to calculate the vertical and horizontal fluxes (Wang et al., 2012a).

Four models include different dust emission/module in this study (Table 1). The M11 model employs the dust mechanism as shown in Eq. S12 (Wang et al., 2017). Besides this, the produced particle servers as places for heterogeneous reactions to take place. Including these reactions can result in extra formation of SO_4^{2-} and NO_3^- in the downwind regions of dust sources. The heterogeneous reactions on dust surface account for almost all of the coarse-mode of NO_3^- and SO_4^{2-} and account for 17% and 11% of fine-mode of secondary NO_3^- and SO_4^{2-} (Wang et al., 2017).

$$F = C_1 \frac{\rho_a}{g} E u^{*3} \left(1 + \frac{u_0^*}{u^*}\right) \left(1 - \frac{u_0^{*2}}{u^{*2}}\right) \left(1 - \frac{RH}{RH_0}\right) \quad (\text{S12})$$

where F is dust flux, C_1 is constant with fixed value of 1.0×10^{-5} , ρ_a is air density, g is gravity acceleration, E is uplifting capability, u^* and u_0^* are friction and threshold friction velocity, RH and RH_0 are relative humidity and its threshold.

M12 and M14 models adopt the same dust module based on dust uplifting theory by (Gillette and Passi, 1988) and modified by (Han et al., 2004). The dust flux is calculated as Eq. S13.

$$F = C' u_0^4 \left(1 - \frac{u_0^*}{u^*}\right) (1 - f_i R_i) \quad (\text{S13})$$

where C' is constant with fixed value of 1.4×10^{-15} , f_i is fractional coverage of vegetation type and R_i is reduction factor, indicating the percentage of dust reduced by vegetation covers in the source region. Studies related to the application of this module can be found in (Ge et al., 2011).

The M10 model uses the online generated dust emission by the GOCART model (Ginoux et al., 2001). The basic approach is also from (Gillette and Passi, 1988), but with different treatment of land types as shown in Eq. S14.

$$F = C'' S s_p u_{10m}^2 (u_{10m} - u_t) \quad (\text{S14})$$

where C'' is constant with fixed value of $1 \mu\text{g s}^2 \text{m}^{-5}$, S is a source function, which is a fraction of alluvium available for wind erosion, indicating the probability to have sediments in grid cell of certain altitude, s_p is fraction of clay and slit for different soil types and u_{10m} and u_t are horizontal wind speed at 10 meters and its threshold.

The sea-salt particles come from breaking waves during coverage of whitecaps over the Open Ocean and coastal surface zone (surf-zone). The impact on aerosol concentration is estimated to extend to at least 25 km in the downwind regions (de Leeuw et al., 2000). Sea-salt emission contributes to 20-40% of SNA and PM_{10} over coastal regions, but the impacts on inland regions is less than 1% (Liu et al., 2015). Including the sea-salt emission in model simulation can improve the model accuracy with 8-20% increase in PM_{10} , SNA, Na^+ and Cl^- (Kelly et al., 2010; Im, 2013). Significant improvements are also found in predicting NO_3^- aerosol over coastal regions (Kelly et al., 2010; Im, 2013).

Similar to dust emission, the sea-salt emissions in models are produced by parameterization. (Neumann et al., 2016) compared the sea-salt emissions from 6 different ways of parameterization from literature. All methods depends on 10 meter wind speed and dry sea-salt particle diameter, but differ with the consideration of salinity (SAL) and sea surface temperature (SST). Besides, one method includes significant wave height and friction velocity at sea surface in the equation.

The M10 and M11 models use the sea-salt parameterization of (Gong, 2003). The production of sea-salt flux over the open ocean is calculate by Eq. (15). The CMAQ model after v4.7 is also equipped with in-line sea-salt emission by (Gong, 2003) and updated by (Kelly et al., 2010). The sea-salt in CMAQ is speciated into three components with fixed proportions: Na⁺ (38.56%), Cl⁻(53.89%) and SO₄²⁻ (7.55%). The non-sodium sea-salt cations (Mg²⁺, Ca²⁺ and K⁺) are treated as Na⁺ equivalents before the CMAQ v5.0. Meanwhile, the CMAQ model adds sea-salt production at surf-zone calculated with Eq. S15, assuming a fixed 100% coverage of whitecap and a 50-meter wide surf-zone.

$$\frac{dF}{dr} = 1.373u_{10m}^{3.41}r^{-A}(1 + 0.057r^{3.45}) \times 10^{1.607e^{-B^2}} \quad (S15)$$

where dF/dr is density function with unit of particles $m^{-2}s^{-2}\mu m^{-1}$, indicating the rate of seawater droplet generation per unit area of sea surface with per increment of particle radius. r is particle radius at RH=80%, u_{10m} is 10 meter wind speed, A is adjustment parameter control the shape of sub-micron size distribution and B is a parameter related to particle radius, calculated as $(0.433 - \log r)/0.433$.

The M12 model adopts the method of breaking wave over coastal sea-zone by (Clarke et al., 2006). The flux is calculated by Eq. S16.

$$S_{100} = \frac{C_s k V_{wind} h}{A_{avg} L + 0.5w_0} \quad (S16)$$

where S_{100} is Sea-salt flux at 100% bubble coverage, C_s is mean braking wave condensation nuclei after vaporize volatile component at 360°C at 5 meters, k is multiplier for tower C_s compared to mean profile, V_{wind} is mean surf-zone wind speed, h is height of plume layer for beach profile, A_{avg} is mean bubble fractional coverage area between wave, L is distance wave travels to shore and w_0 is initial width of breaking wave bubble front.

S1.3 Removal mechanisms: wet and dry deposition

Wet and dry depositions are the common ways to remove particles from the atmosphere in models. The removal pathways may be different depending on the size of particles. The coarse-mode particles are removed by sedimentation/dry deposition, while the fine-mode particles are more easily cleared by wet deposition.

Wet deposition is the removal pathway of gases and aerosols by rain droplets, involving both in-cloud scavenging (rainout) and below-cloud scavenging (washout). The gases in the atmosphere are dissolved in the raindrop and are removed from the atmosphere. For the non-reactive gases, the removal rate depends on the solubility of gases and is a function of the Henry's Law. Particles participate in the cloud condensation nuclei in the presence of supersaturation water

vapor and then grow into cloud droplets. The efficiency is assessed by so-call “washout ratio”, calculated as the ratio of particle concentrations in deposition to particle concentrations in surface air as shown in Eq. 3 (also shown in manuscript).

$$\lambda_{wet} = \frac{C_{depo}}{C_{surface_air}} \times 100\% \quad (3)$$

where λ_{wet} is the washout ratio for wet deposition, C_{depo} is the concentration of particles in deposition and $C_{surface_air}$ is the concentration of particles at near surface atmosphere.

Dry deposition removes aerosols by gravitation. In this study, all models except M12 use the same dry deposition scheme from (Wesely, 1989). The dry deposition flux is proportional to the concentration of pollutants at height. The dry deposition velocity is calculated with Eq. 4 (also shown in manuscript).

$$V_d = -F_c / C_a \quad (4)$$

where F_c is the dry deposition flux, V_d is the deposition velocity and C_a is the concentration of species at height. The negative mark indicates the direction of the dry deposition velocity. The V_d is determined by the resistance of air layer (r). The total r is composed of three factors (Eq. S17): the aerodynamic resistance (r_a), boundary layer resistance (r_{bc}) and canopy resistance (r_{surf}).

$$V_d = \frac{1.0}{r_{surf} + r_a + r_{bc}} \quad (S17)$$

The M12 predicts dry deposition velocity with the general approach from (Wesely, 1989) with updates by (Zhang et al., 2003). The study updates the value of non-stomatal resistance (R_{ns}), which is a component of R_{surf} related to the soil uptake and cuticle uptake of dry deposition. Model evaluation shows the updates changed the model prediction of dry deposition velocities of SO_2 (Zhang et al., 2003).

S2. Model evaluation

The MMM performances on PM_{10} , $PM_{2.5}$, SNA and AOD over EA are evaluated with observation. The main purposes are to investigate the discrepancies between model and observation and identify possible reasons for the model bias. This section shows the differences between MMM and observation and the inter-model variations (1sd and 1sd%). To make the discussion clear, we define the regions used in the following analysis here: northern EA (Russia and Mongolia), central EA (China), western EA (Japan and Korea) and southern EA (Cambodia, Lao PDR, Myanmar, Thailand, Vietnam, Indonesia, Malaysia and Philippines). Since M14 model has a smaller simulation domain than the others, it is not included in the MMM results in this section.

S2.1 Observation data and model evaluation metrics

Figure S1 shows the locations of observation sites in this study. A1-A86 (red) are 86 sites from the Air Pollution Indices (APIs) with monthly average PM_{10} data (<http://datacenter.mep.gov.cn/>). This dataset has been widely used to study the PM pollution (Qu et al., 2010; Chen et al., 2008; Deng et al., 2011) as well as model evaluation (Wang et al., 2012b; Xing et al., 2015) in

China. It is replaced by the Air Quality Index (AQI) after 2013. The APIs data covers the eastern China with intensively located sites, but the number of sites in western China is very limited. E1-E54 (blue) are 54 sites from EANET (<http://www.eanet.asia/>, last access: 28 May 2018). This network provides monthly average concentrations of PM₁₀, SNA and S and N depositions. The data quality is checked that sites with less than 80% completeness (i.e. <24 days in a month) are not used for evaluation. Only sites with qualified data during the research time are shown in fig. S1. This dataset covers the eastern EA (Japan and Korea) and Southeast Asia well with PM₁₀ observation. There are also some sites in northern EA, but the data completeness is not as satisfied as the other sites. Meanwhile, the number of Chinese site is limited. The Chinese sites are generally located along the east coast of China and couldn't well cover the areas with high PM₁₀ pollution, such as the Hebei-Beijing-Tianjin (HBT) region. This dataset also provides PM_{2.5} observation, but only three sites located in Rishiri (E15), Ochiishi (E16) and Oki (E21) in Japan are available during our study period. These three sites are located in the remote regions of Japan and couldn't represent the high pollution in the urban regions. R1-R35 (green) are 35 Reference (Ref) sites provided by the Institute of Atmospheric Physics Chinese Academy of Science (IAP_CAS). The sites are intensively located in three regions: HBT region, Pearl River Delta (PRD) and Taiwan. Monthly average concentrations of PM₁₀ and PM_{2.5} are available for evaluation.

We also evaluate the model performance on aerosol optical depth (AOD) with observation data from AErosol RObotic NETwork (AERONET) (<https://aeronet.gsfc.nasa.gov/>, last access: 28 May 2018) and Moderate Resolution Imaging Spectroradiometer (MODIS) (<https://modis-atmos.gsfc.nasa.gov/>, last access: 28 May 2018). The AERONET network is global-wide ground-based remote sensing monitoring network for aerosols. This study uses the version-3 level-2 AOD product with quality assurance. There are altogether 61 sites during the research period, but the data completeness is not satisfying for most sites. Some sites even have one day of observation in a month. In order to ensure the quality of observation data, we only use data with at least 20 days of observation available in one month (2/3 completeness). After the quality check, only data from 16 sites can be used for evaluation. The location of sites are marked in fig. S6. The MODIS data is remote sensing data derived from the Terra and Aqua satellites. This study uses the MODIS level-2 atmospheric aerosol product of AOD at 550 nm from Dark Target (DT) and Deep Blue (DB) algorithms.

S2.2 Spatial distribution evaluation

Figure S3 compares the MMM results with observation for annual average concentrations of surface PM₁₀, PM_{2.5} and SNA. Table 2 summaries the statistical metrics of MMM performance. Overall, the MMM underestimates the PM₁₀ and PM_{2.5} concentrations by 25 $\mu\text{g m}^{-3}$ (30%) and 7 $\mu\text{g m}^{-3}$ (15%). The model bias for SNA are -0.7 $\mu\text{g m}^{-3}$ (-19%), -0.05 $\mu\text{g m}^{-3}$ (-3%) and 0.1 $\mu\text{g m}^{-3}$ (12%) for SO₄²⁻, NO₃⁻ and NH₄⁺, respectively. Following are the analysis of MMM performance for different datasets and regions.

For central EA, the north China is observed with the highest PM₁₀ concentrations and the MMM could well reproduce them except the HBT region and the northwest China (fig. S3(a)). Large model underestimation of PM₁₀ (40 $\mu\text{g m}^{-3}$ (300%)) is found in northwest China, despite the very limited number of observation sites. The PM₁₀ at the HBT sites is also largely underestimated

by $68 \mu\text{g m}^{-3}$ (46%). The biases for individual sites range from -13% to -77%, indicating a systematic model underestimation at all sites in this region. On the contrary, the $\text{PM}_{2.5}$ at these sites are generally well simulated with much lower bias ($-7.6 \mu\text{g m}^{-3}$ and -11%). Since the number of sites for $\text{PM}_{2.5}$ (8) is less than that for PM_{10} (18), we analyse the seven sites with both PM_{10} and $\text{PM}_{2.5}$ observation (one of the eight sites only has $\text{PM}_{2.5}$ observation). The PM_{10} bias are $-58.4 \mu\text{g m}^{-3}$ (-42%) and the $\text{PM}_{2.5}$ bias are $-9.2 \mu\text{g m}^{-3}$ (-12%). The much lower $\text{PM}_{2.5}$ bias than PM_{10} bias suggests model underestimation of coarse-mode of particle (PMC), probably related to dust emission. In east and south-central China, the MMM underestimates the PM_{10} concentrations at the APIs sites by about $30\text{-}40 \mu\text{g m}^{-3}$ (50-100%), in particular at the sites along the east coast of China. At the PRD sites, the PM_{10} is underestimated by $23.2 \mu\text{g m}^{-3}$ (34%) and the $\text{PM}_{2.5}$ is underestimated by $6.8 \mu\text{g m}^{-3}$ (17%). We compare the three sites with both PM_{10} and $\text{PM}_{2.5}$ observation. The MMM underestimates the PM_{10} by $23.2 \mu\text{g m}^{-3}$ (39%), $24.8 \mu\text{g m}^{-3}$ (34%) and $12.6 \mu\text{g m}^{-3}$ (26%), respectively, and underestimates the $\text{PM}_{2.5}$ by $5.9 \mu\text{g m}^{-3}$ (16%), $9.8 \mu\text{g m}^{-3}$ (20%) and $6.4 \mu\text{g m}^{-3}$ (18%), respectively. Similar to the HBT regions, underestimation of PMC is found in this region, but the bias is relatively lower than that of HBT region. In case of SNA, only site E6 located on Xiamen Inland in south-central China is available. This site is largely underestimated by 50-60% for SNA. Overall, the sites located near the coastal region are somewhat underestimated.

For eastern EA, the MMM underestimates the PM_{10} by $14.6 \mu\text{g m}^{-3}$ (52%). The ten Japanese sites are underestimated by $11.7 \mu\text{g m}^{-3}$ (49%). The three Korean sites are underestimated by $24.1 \mu\text{g m}^{-3}$ (52%). In case of $\text{PM}_{2.5}$ and SNA, only observations from the Japanese sites are available. The $\text{PM}_{2.5}$ at the Japanese sites are underestimated by $4.3 \mu\text{g m}^{-3}$ (40%). For SNA, the model bias of Japanese sites are $-0.7 \mu\text{g m}^{-3}$ (-22%), $0.2 \mu\text{g m}^{-3}$ (21%) and $0.1 \mu\text{g m}^{-3}$ (11%) for SO_4^{2-} , NO_3^- and NH_4^+ , respectively. The SO_4^{2-} concentrations are underestimated at all sites (except E19), while there are both positive and negative model bias for NO_3^- and NH_4^+ . We pick out the two sites (E15 and E21) with complete observation of PM_{10} , $\text{PM}_{2.5}$ and SNA. The model biases are -40% and -58% for PM_{10} , -33% and -33% for $\text{PM}_{2.5}$, -30% and -35% for SO_4^{2-} , 14% and -27% for NO_3^- and 1% and -24% for NH_4^+ . The underestimation of SO_4^{2-} could relate to the oxidation of SO_2 . Another possible reason for the model bias is the complicated geographical location of sites. The E19 site, located in 1850 meters high, is found with large model bias of 209%, 630% and 223% for SNA. The E23 site, located on 790 meters high, is found with lower model bias: -28%, 225% and 24% for SNA, but its bias are still among the highest of all sites.

For northern EA, the SNA observation is available at five sites. The model bias of SNA are $-1.2 \mu\text{g m}^{-3}$ (-47%), $0.1 \mu\text{g m}^{-3}$ (16%) and $0.1 \mu\text{g m}^{-3}$ (12%) for SO_4^{2-} , NO_3^- and NH_4^+ , respectively. The bias of individual sites varies largely for SO_4^{2-} (-80% to 36%), NO_3^- (-73% to 220%) and NH_4^+ (-82% to 58%). This region has been identified with poor quality in the emission inventory compared with other regions in the study of MICS-Asia II (Carmichael et al., 2008). In this study, the emissions of this region come from the Regional Emission Inventory in Asia (REAS) version 2.1 (Li et al., 2017). The base year of the inventory is 2000-2008, not extended to the simulation year of 2010. This database serves as the default emission inventory for regions with no local emission information as update. The large model bias found in this study indicates update in emissions is required to improve model accuracy. Furthermore, Russian emission has

been reported with high uncertainties (Huang, 2014;Kholod et al., 2016), and recent studies were trying to identify the missing emission sources such as gas flaring (Huang et al., 2015) and reconstruct the emissions such as biomass burning (Hao et al., 2016) and diesel combustion (Kholod et al., 2016). The updated emissions with localized data could be 10 times higher than the global-wide emission inventories (Hao et al., 2016). For southern EA, only three observation sites in Thailand are available for PM₁₀, which are all slightly underestimated by about 15-20 $\mu\text{g m}^{-3}$ (42-47%). The model biases at these sites are 0.5 $\mu\text{g m}^{-3}$ (14%), 0.4 $\mu\text{g m}^{-3}$ (28%) and 1.2 $\mu\text{g m}^{-3}$ (124%) for SO₄²⁻, NO₃⁻ and NH₄⁺, respectively. But since no sites has a complete set of observation data for both PM₁₀/PM_{2.5} and SNA, it is hard to provide a comprehensive review in this region.

Figure S4 shows the inter-model variations of surface PM₁₀, PM_{2.5} and SNA among all participating models. The 1sd and 1sd% of PM₁₀ can reach upmost 80-90 $\mu\text{g m}^{-3}$ and 200%, respectively (fig. S4(a-b)). The model results are consistent over oceans (1sd <10 $\mu\text{g m}^{-3}$) and coastal regions (1sd ~10 $\mu\text{g m}^{-3}$). For inland regions, the models have higher agreement in east China, eastern EA and southern EA (1sd <10 $\mu\text{g m}^{-3}$ and 1sd% =10-30%) than the other regions. The HBT region is attributed by model discrepancies of 10-20 $\mu\text{g m}^{-3}$ (10-30%). This is relatively low compared to the model underestimation of PM₁₀ in this region (68 $\mu\text{g m}^{-3}$ and 46%). This supports our suspect of systematic underestimation in this region by most models as analysed above. The highest inter-model discrepancies are found in northwest China, especially around the Taklimakan and Gobi Deserts (100-110 $\mu\text{g m}^{-3}$ and >210%), due to the implementation of dust emission in four of the twelve models. Similar distribution patterns are found in PM_{2.5} (fig. S4(c-d)). The spatial distributions of SNA (fig. S4(e-j)) are considerably different from those of PM₁₀ and PM_{2.5}. The models have higher consistency in SNA than PM₁₀ and PM_{2.5} in northwest China. The inter-model differences in eastern China are higher for SNA (40-60%) than PM₁₀ and PM_{2.5} (10-30%). This is because that eastern China is distributed with intensive emissions of SNA precursors (i.e. SO₂, NO_x and NH₃) (Li et al., 2017). In addition, some regions with high variations are worth-noting here. Japan is attributed with higher inter-model variations of SO₄²⁻ than the other regions (90-100%). South EA is found with high inter-model differences in NO₃⁻ concentrations (60-100%). The variation of NO₃⁻ is extremely high on the open ocean (80-100%), which is related to the treatment of sea-salt emissions in model simulations.

S2.3 Temporal distribution evaluation

Figure S5 compares the monthly variations of PM and its components between MMM and observation. The MMM results and observations are the average concentrations of all corresponding sites of the datasets/regions. The inter-model variations (1sd) are presented with the grey-shaded areas. For central EA (fig. S5(a-d and h)), the trends of PM₁₀ are generally well simulated with high R values (~0.9) except the HBT region (0.5). However, the magnitudes of PM₁₀ are generally underestimated in all months in all datasets except the EANET site (fig. S5(h)). Among all regions, the largest model bias is found in the HBT region, where the modeled PM₁₀ are 50 $\mu\text{g m}^{-3}$ lower than the observation in most months. Among the twelve months, the model bias is highest in March-May (spring season) and November-January (winter season) for all sites. For the HBT region, the MMM underestimates the PM₁₀ concentration peak in March, probably due to lack of dust emissions in some models. For the API sites, the MMM fails to predict the high

concentration in March. The inter-model variation is high in this month, which means that some models can reproduce this characteristic. For PRD and Taiwan, the MMM produces concentration peaks in March, but underestimates the magnitudes. In case of PM_{2.5}, both the monthly trends and concentrations are well captured by MMM in the HBT and PRD regions, which is different from PM₁₀. This again supports our suspect that the model bias in simulating PM₁₀ over the HBT region can be attributed to model bias in PMC. On the other hand, the PM_{2.5} at Taiwan sites are underestimated by about 10-20 $\mu\text{g m}^{-3}$ in all months, which is the similar amount to the model underestimation of PM₁₀ in this region. The MMM misses the concentration peak of PM_{2.5} in March, also similar with PM₁₀. Different from the HBT region, the model bias in this region comes from model treatment of fine-mode of particles. Only one EANET site is available for SNA, therefore further evaluation is required before drawing a concluding. The magnitudes of SNA are poorly simulated by MMM despite high R values of NO₃⁻ (0.85) and NH₄⁺ (0.85). In particular, the MMM has largely underestimated the high concentrations of SNA during November to April.

For northern EA, the observed SO₄²⁻ shows two concentration peaks throughout the year: a 6-month peak from November to April and a single-month peak in June. The modelled SO₄²⁻ shows an opposite trend with the observation (R = -0.64). Since the 1sd is low, this is considered as a systematic model bias for SO₄²⁻ in this region. The modelled NO₃⁻ and NH₄⁺ have high R values with observation. The concentrations of NO₃⁻ are well caught by MMM, especially the peaking values during November-April. The concentrations of NH₄⁺ are largely underestimated during winter and spring. In addition, both modelled NO₃⁻ and NH₄⁺ have high inter-model variations during winter, when the observed concentrations are high. For southern EA, the observed PM₁₀ peaks in March and November. The MMM has well reproduced this trend, but underestimates the peaking concentrations in both peaks. Beside this, the other months are generally under-predicted by about 10 $\mu\text{g m}^{-3}$. In case of SNA, the modelled trends and concentrations of SO₄²⁻ agree well with observation in most months except February-March. The observed SO₄²⁻ peaks from February, but the MMM peaks one month later. The MMM has largely underestimated the NO₃⁻ concentrations during March-May and NH₄⁺ concentrations in May. This is because 1 site in Thailand has much higher observed NO₃⁻ (68 $\mu\text{g m}^{-3}$) and NH₄⁺ (7 $\mu\text{g m}^{-3}$) than the other sites, but the MMM fails to catch this site. This underestimation is not found in SO₄²⁻ because this site doesn't provide SO₄²⁻ observation.

For eastern EA, the observed PM₁₀ shows two peaks at the same episode as southern EA. But the modelled monthly trend of PM₁₀ is almost flat throughout the year. The PM₁₀ concentrations are generally underestimated by 10-20 $\mu\text{g m}^{-3}$, especial during the two peaking periods. The trend of PM_{2.5} is also poorly simulated with R of 0.02, due to underestimation of concentrations during April to June. It should be noted that the number of PM_{2.5} observation sites (3) is much lower than that of PM₁₀ (13), and the observation sites of PM_{2.5} are all located in the remote regions of Japan. Therefore, it could be inappropriate to relate the evaluation results of PM_{2.5} with those of PM₁₀. In case of SNA, the MMM has well simulated both the trends and concentrations of NH₄⁺, but performed poorly on SO₄²⁻ and NO₃⁻. The SO₄²⁻ concentrations are underestimated during January-March, and the modelled trend of NO₃⁻ is almost opposite to the observation during May-July. It is worth-noting that the inter-model variations of SO₄²⁻ and NO₃⁻

in this region are considerably high throughout the whole year, and the 1sd values are the highest among all EA regions. The possible reason may lay on model formation of fine particles.

S2.4 Model performance on AOD column

This section compares the modelled monthly AOD at mid-visible (500 nm) with observation. Figure S6 shows the comparison of MMM results with AERONET and MODIS at the AERONET sites. The inter-model differences (± 1 sd) are also shown with grey-shaded areas. The AERONET data is discontinued due to data incompleteness (mention in sect. S2.1), which makes it difficult to assess the temporal variation. The model results of M5 and M6 are not available and the results of M7, M8, M12 and M13 are unreasonable. Therefore, only model results of M1, M2, M4, M10 and M11 are used. For central EA, observation from five sites are available for comparison. The Xinglong and Xianghe sites are located close to each other in northeast China. The modelled AOD at the Xianghe site agrees well with the observations from both AERONET and MODIS. The AOD at the Xinglong site is overestimated during July-September. The SACOL site is located in northwest China. The MMM agrees well with both observation datasets during October-December, but misses the high concentrations in April. The NAM_CO and QOMS_CAS sites are located in southwest China. Very limited AERONET data is available at these two sites. The Issyk-Kul and Dushanbe sites are located close to the Taklamakan Desert. The AOD at the Dushanbe site is 50% lower than the AERONET data during July and December. The MMM fails to reproduce the concentration peak in August and the increasing trend from September to December. The Issyk-Kul site only has AOD observation in August and the value is slightly overestimated by MMM. Eight sites are available for southern EA. The five Indian sites are all located close to the Himalayas Mountain: Lahore, Karachi, Nainital, Kanpur and Kathmandu_ Univ. The Nainital and Kathmandu_ Univ sites are well simulated with slight overestimation during September-December. The Lahore site is generally underestimated in all months. The Kanpur site is underestimated during April-June, but it is well simulated during October-March. The modelled AOD in the Karachi site fits well with the MODIS data, but is lower than the AERONET data. The two sites in Thailand (Chiang_Mai_Met_Sta and Silpakorn_ Univ) are generally underestimated, especially in March and August. The AOD in the Manila Observatory site in Philippine is well simulated in February and March. For eastern EA, the AOD in the Ussuriysk site is overestimated during July-October.

Figure S7 compares the spatial distribution of modelled AOD with MODIS satellite data in four seasons (Dec-Feb as winter). The MODIS data shows several hot spots in central EA and southern EA, especially the HBT region (0.6-0.9), south-central China (~ 0.6), Sichuan Province (~ 0.8) and around the Himalayas Mountain (0.5-0.6). These patterns are generally well reproduced by MMM. The AOD values in south-central China are somewhat overestimated by MMM in Spring and Fall, while the AOD values around the Himalayas Mountain are underestimated in Spring and Summer. In spring, the MODIS detects very high AOD around the Taklamakan Desert (0.6-0.9), but the MMM fails to simulate it and produces as low value as the background AOD (~ 0.2). According to 1sd plot, this region has about ± 0.2 disagreement on AOD among models, due to M10, M11 and M14 models produce higher AOD than the other models owing to the implementation of dust emissions in simulations. South China is attributed with the highest 1sd

among all regions (± 0.5), due to M2 and M10 models produce higher AOD than other models and MODIS. Overall, we get consistent evaluation results by comparing model results with AERONET and MODIS. The AOD in north-western EA (near Taklamakan desert) and southern EA (around the Himalayas Mountains) is somewhat underestimated, while that in central and eastern EA is generally well simulated. The seasonal comparison with MODIS further confirms the model underestimation of AOD in north-western EA during the spring season, which is close related to dust emissions.

S2.5 Model performance on wet deposition

We evaluate the model performance on wet deposition with observation as shown in fig. S8. The statistical metrics are listed in Table S1. For wet SO_4^{2-} deposition, despite that the two highest sites (E2 and E3) in China are underestimated, the other sites are generally well simulated by MMM with a MB of -8%. The individual model bias vary from -22% to 41%. The CMAQ models (M2, M4 and M6) all underestimate the wet SO_4^{2-} deposition. There are large differences between CMAQv4.7.1 and CMAQv5.0.2 in JP, where the CMAQv4.7.1 models (M4 and M6) slightly overestimate the wet SO_4^{2-} deposition at E19 and E23, while the CMAQv5.0.2 model (M2) slightly underestimates the value at these sites. The M11 and M12 models produce considerably different results with the CMAQ models, especially in east EA.

The MMM underestimates the NO_3^- wet deposition by 29%, due to large under-prediction in southern EA. The southern EA has several sites with very high deposition, such as E29 site in MY and E35 and E36 sites in PH, but all models fail to catch those high peaks. The individual model bias varies from -59% to 30% among models. M2, M4, M6 and M12 perform similarly with high underestimation ranging from 39% to 59%. The M11 is the only model that succeed to capture the high wet NO_3^- deposition at E2 and E3 in CH, but it overestimates most sites in CH, JP and KR.

In case of wet NH_4^+ deposition, the MMM generally underestimates the amount at all sites with a bias of -40%, especially at E2-E4 in CH, E45 in TH and E35 and E36 in PH. The individual model bias varies from -10% to -37%. The M2, M4 and M6 models perform similarly, while M11 and M12 models predict higher depositions at all sites. The observation of dry deposition is composed by observed concentration of air pollutants and simulated deposition velocity. Since the EANET network only provides the former one, we are unable to evaluate the dry deposition in this study (complete dry deposition with velocity is available after 2013).

Supplementary figures

Figure S1

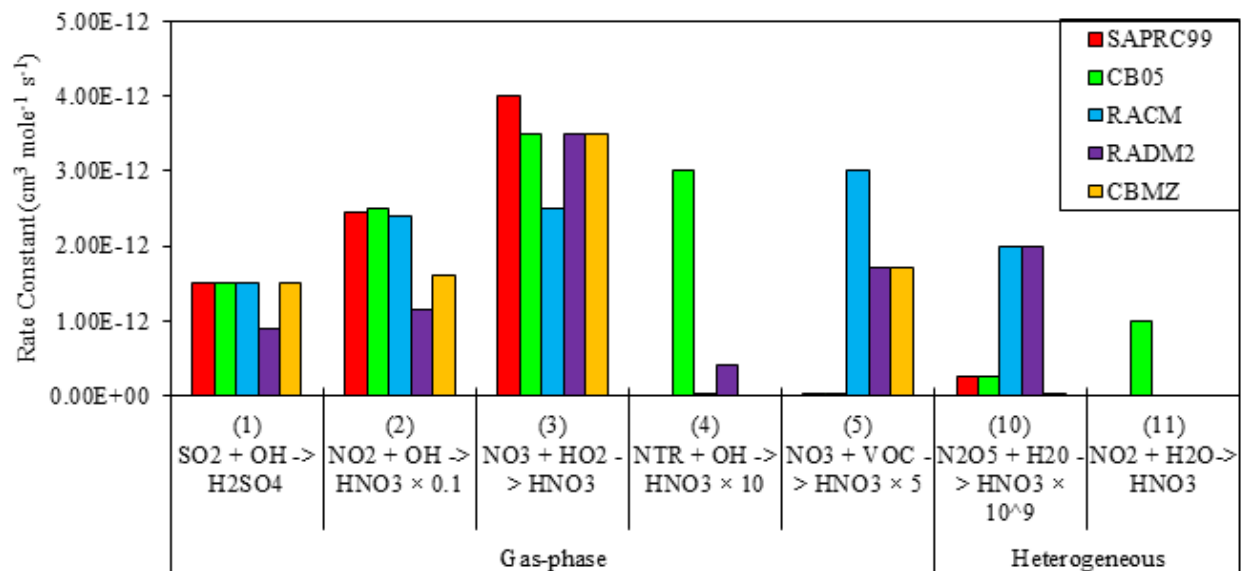


Figure S1 Major reaction rates of the formation of SO_4^{2-} and NO_3^- at 298K and 1atm. The rate of some reactions are scaled as indicated. PAN is used to represent NTR in the reaction of $\text{NTR} + \text{OH}$. HCHO is used to represent VOC in the reaction of $\text{NO}_3 + \text{VOC}$.

Figure S2

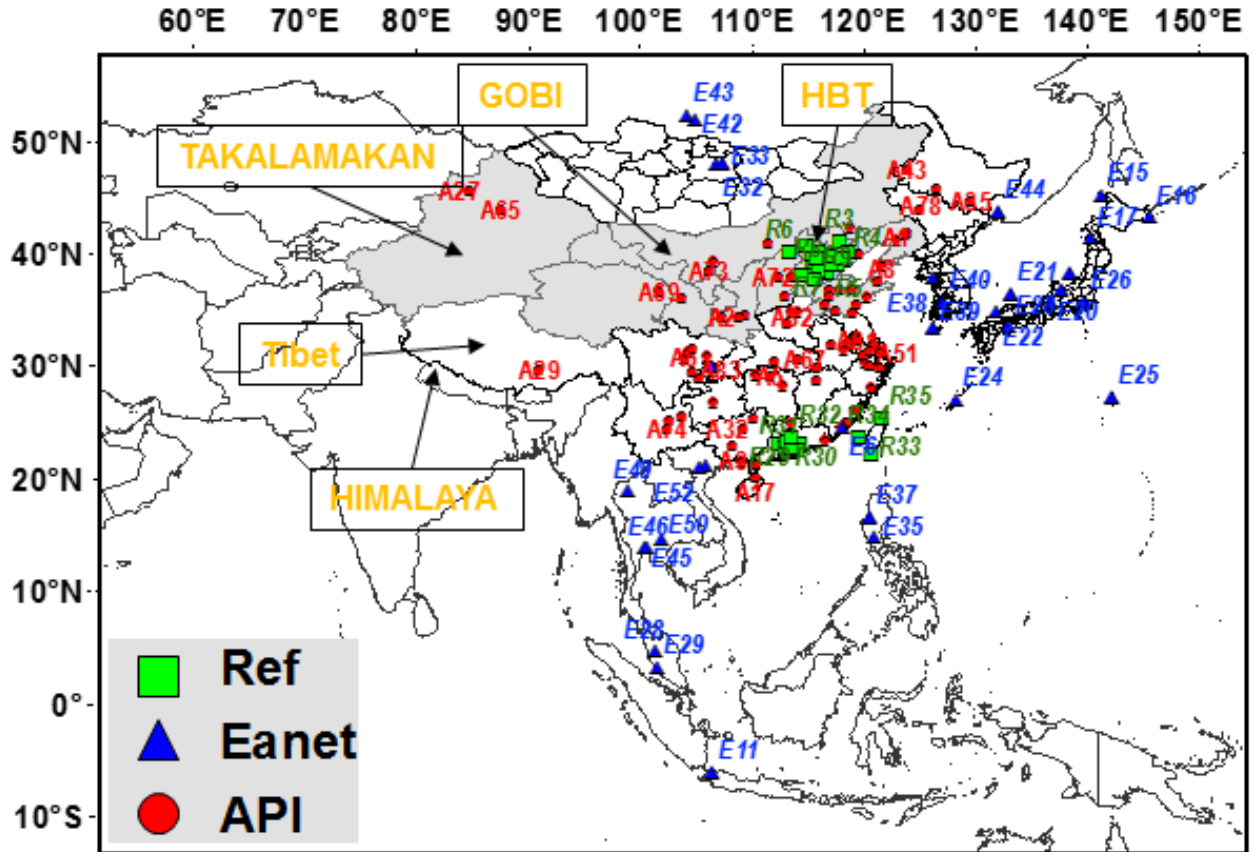


Figure S2 The geographical locations of observation networks of API (red color, A1-A86), EANET (blue color, E1-E54, only sites with available observation during simulation time are shown) and Ref (green color, R1-R35) sites. Grey shaded regions have been reported to be affected by dust storms.

Figure S3

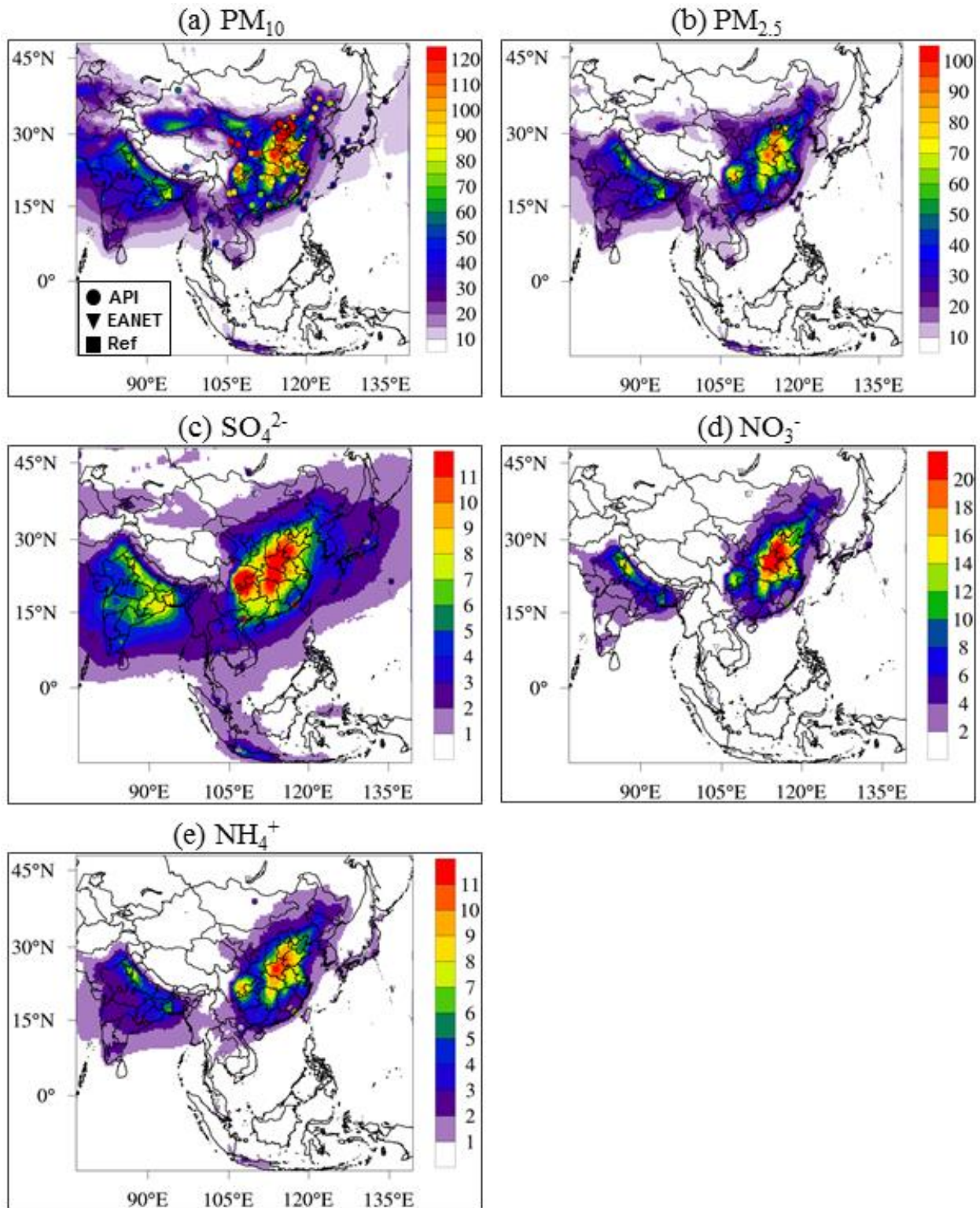


Figure S3 Comparison of annual average concentrations of PM and components from MMM (contour) with observation (markers). Unit: $\mu\text{g m}^{-3}$.

Figure S4

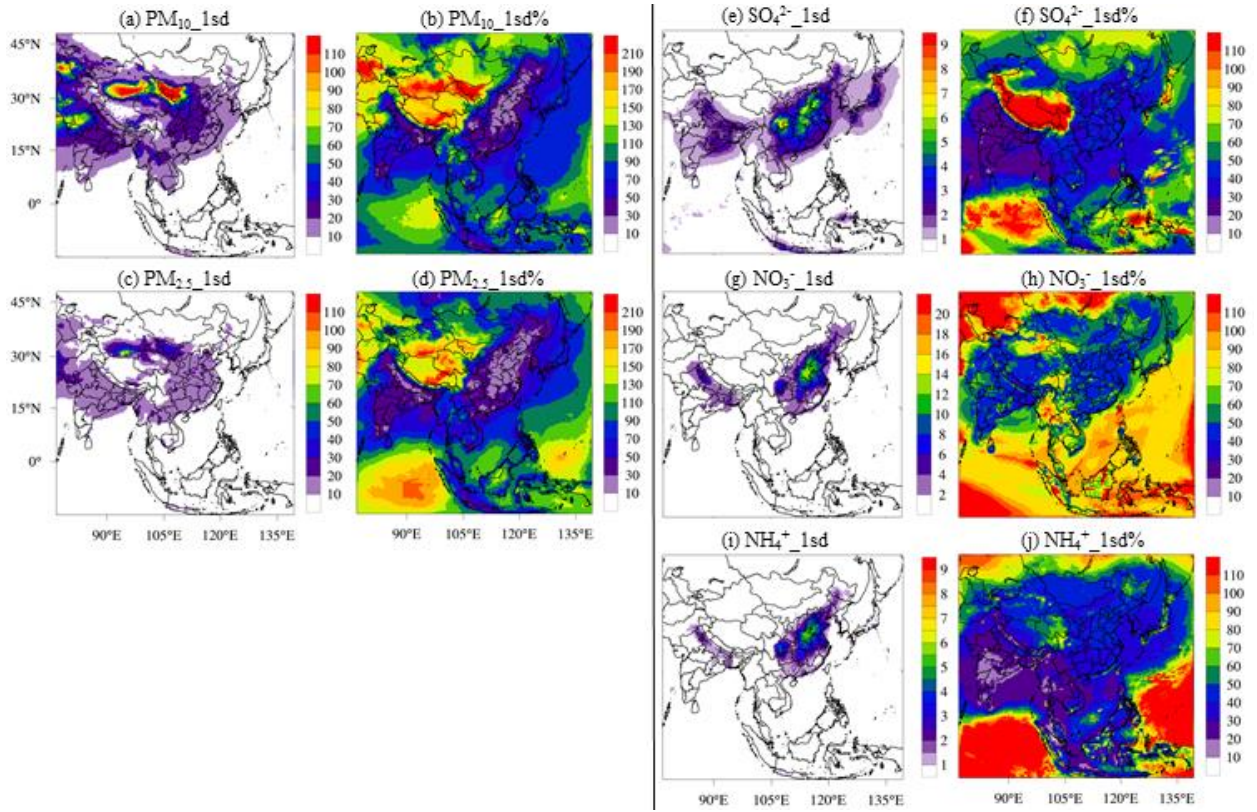


Figure S4 The inter-model variations of PM and components among models. The 1sd is the 1 standard deviation among models ($\mu\text{g m}^{-3}$). The 1sd% is calculated by dividing 1sd by MMM (%).

Figure S5

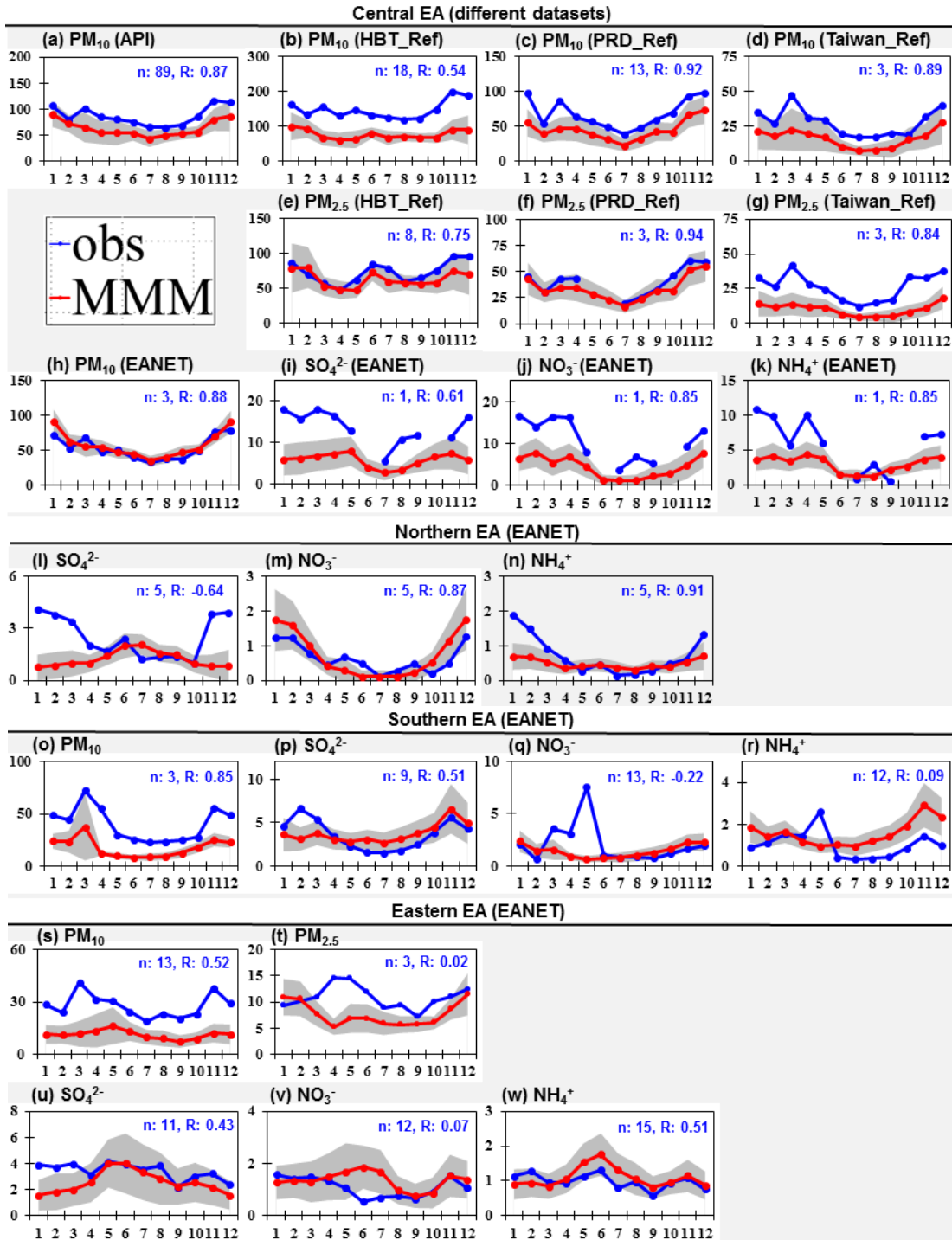


Figure S5 Monthly average concentrations of PM and components from MMM (red line) and observation (blue line) ($\mu\text{g m}^{-3}$). The grey-shaded areas are ± 1 sd of models. The upper-right values are the numbers of sites (n) and the correlations (R) between model and observation.

Figure S6

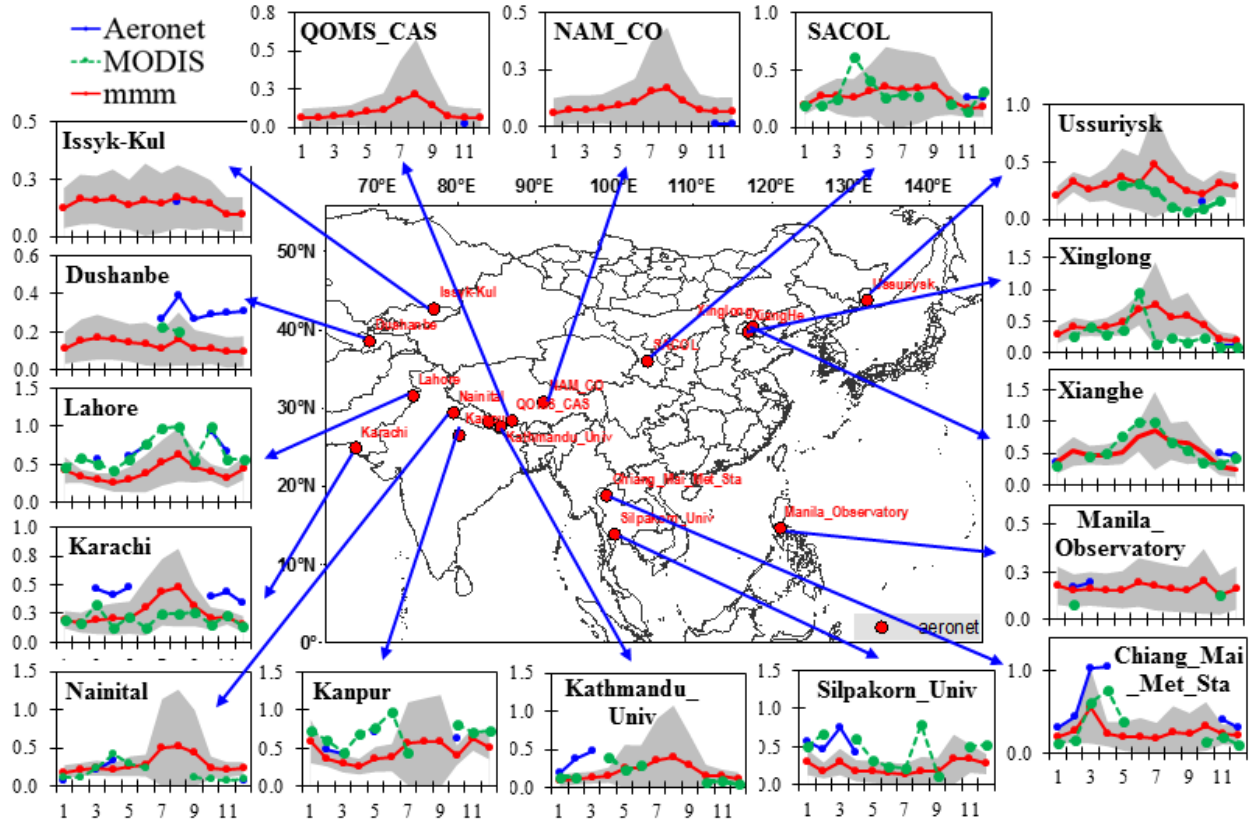


Figure S6 Monthly average AOD from MMM (red line) and observation from Aeronet (blue line) and MODIS (green). The x axis presents the months. The grey-shaded areas are ± 1 sd of models.

Figure S7

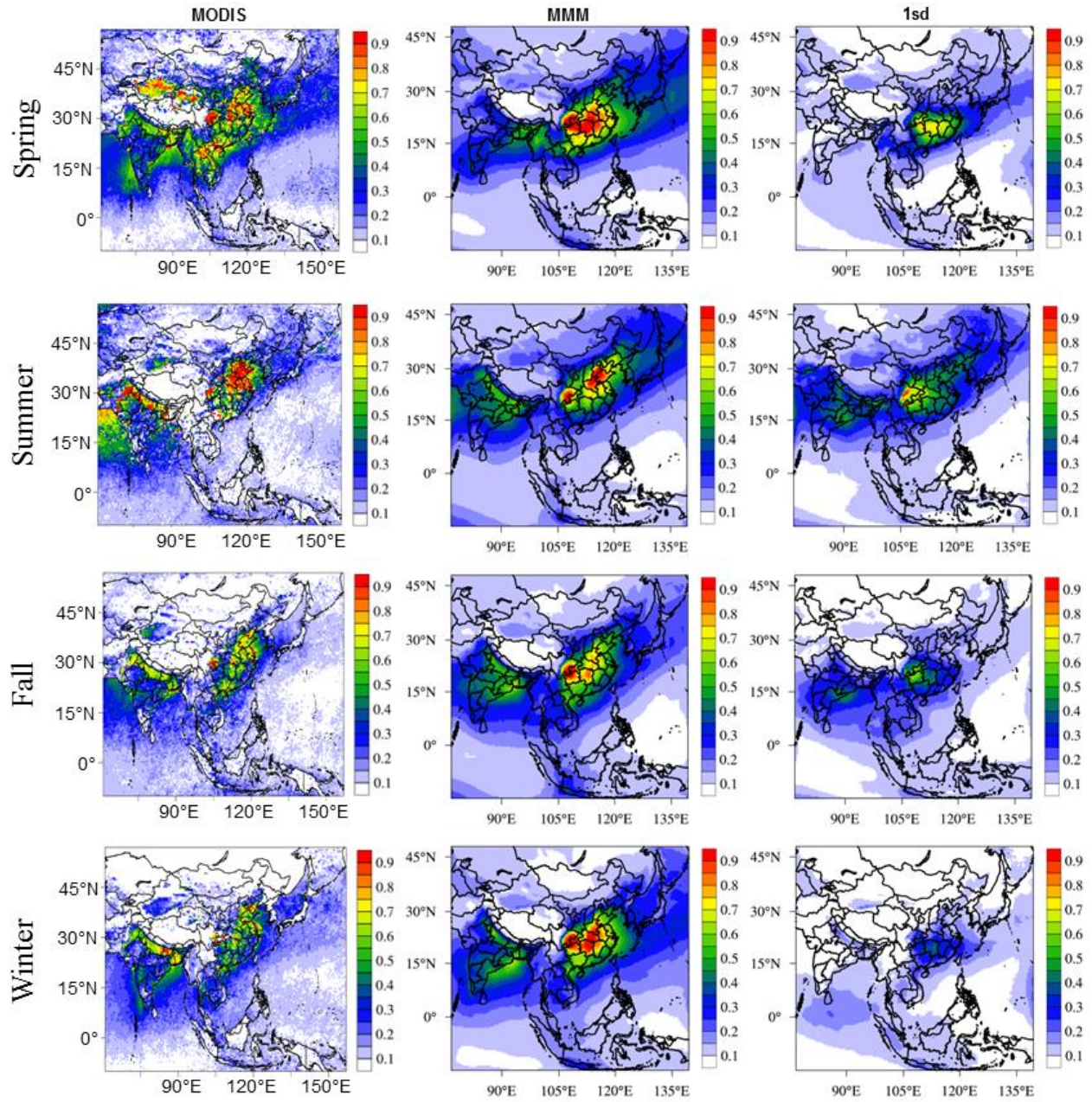


Figure S7 (Left 2 columns) Comparison of seasonal average AOD values between MMM and MODIS data. (Right column) +1 sd among models.

Figure S8

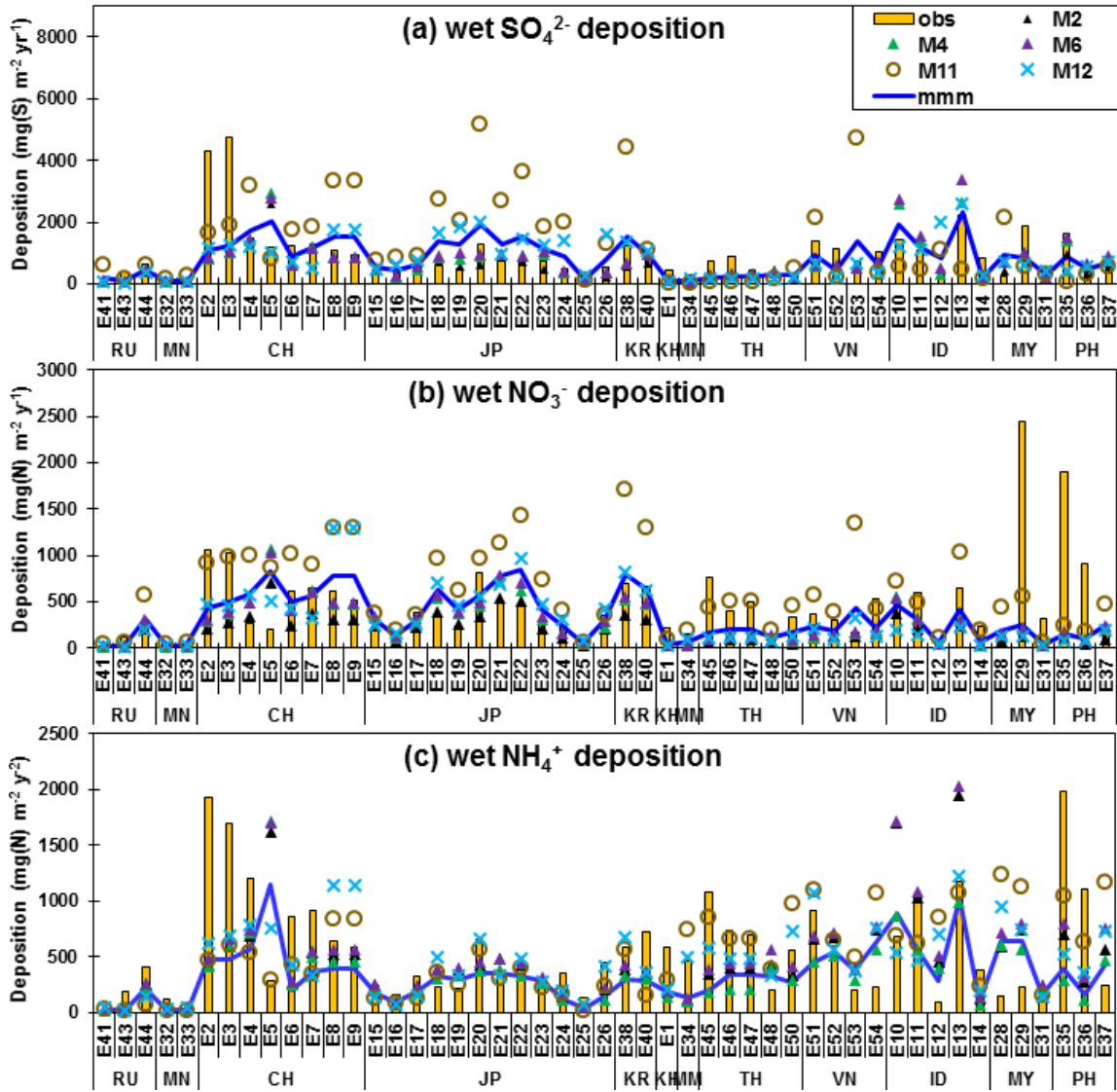


Figure S8 Modelled annual-accumulated wet deposition of SO_4^{2-} , NO_3^- and NH_4^+ compared with observation from EANET network. The units are mg(S or N) m⁻² yr⁻¹. Abbreviation for regions: RU-Russia, MN-Mongolia, CH-China, JP-Japan, KR-Korea, KH-Cambodia, MN-Myanmar, TH-Thailand, VN-Vietnam, ID-Indonesia, MY-Malaysia, PH-Philippine.

Figure S9

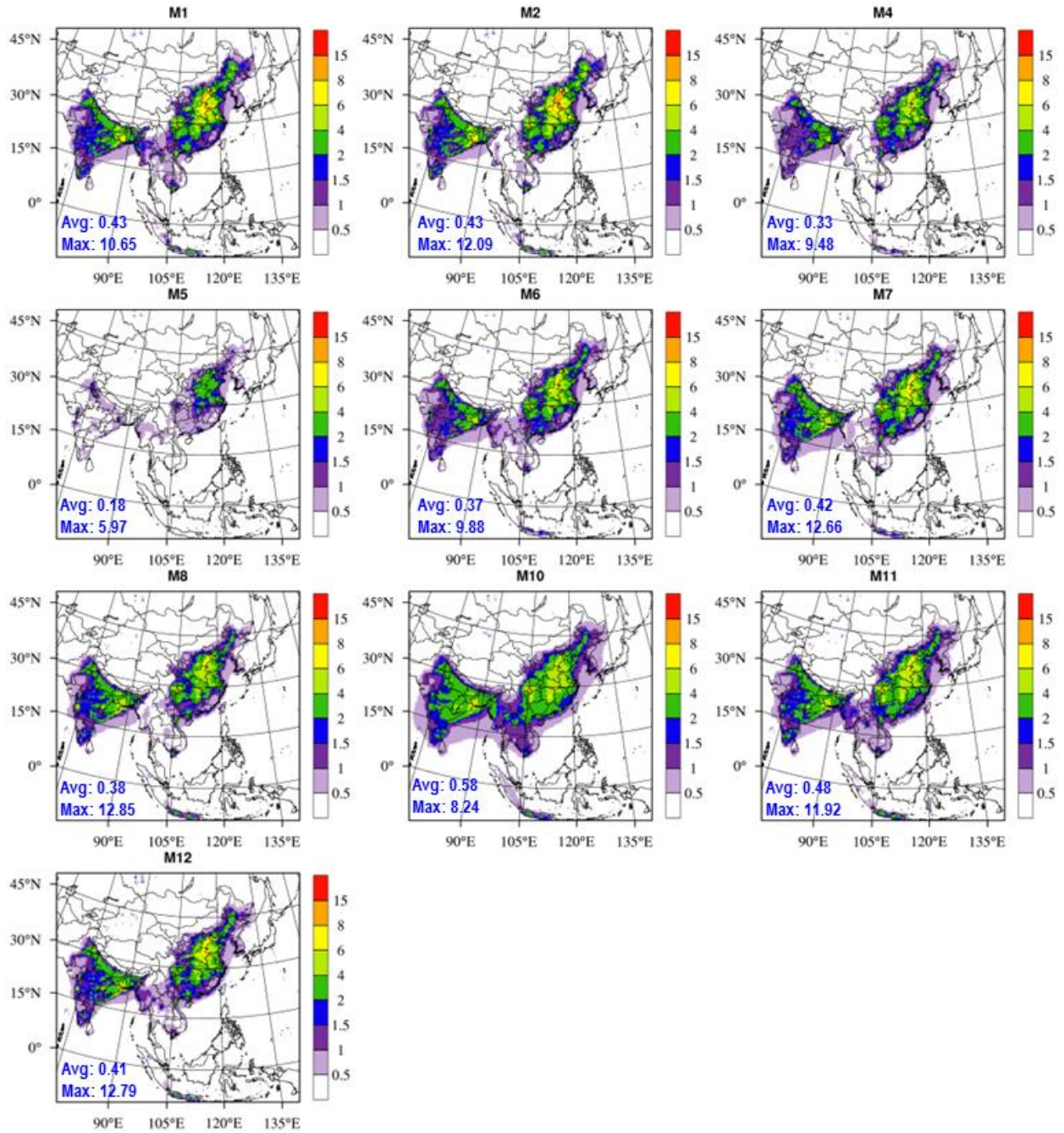


Figure S9 Surface BC concentrations of models (unit: $\mu\text{g m}^{-3}$). Values are calculated by annual average data. The bottom-left values are domain average (Avg) and domain maximum (Max) concentrations.

Figure S10

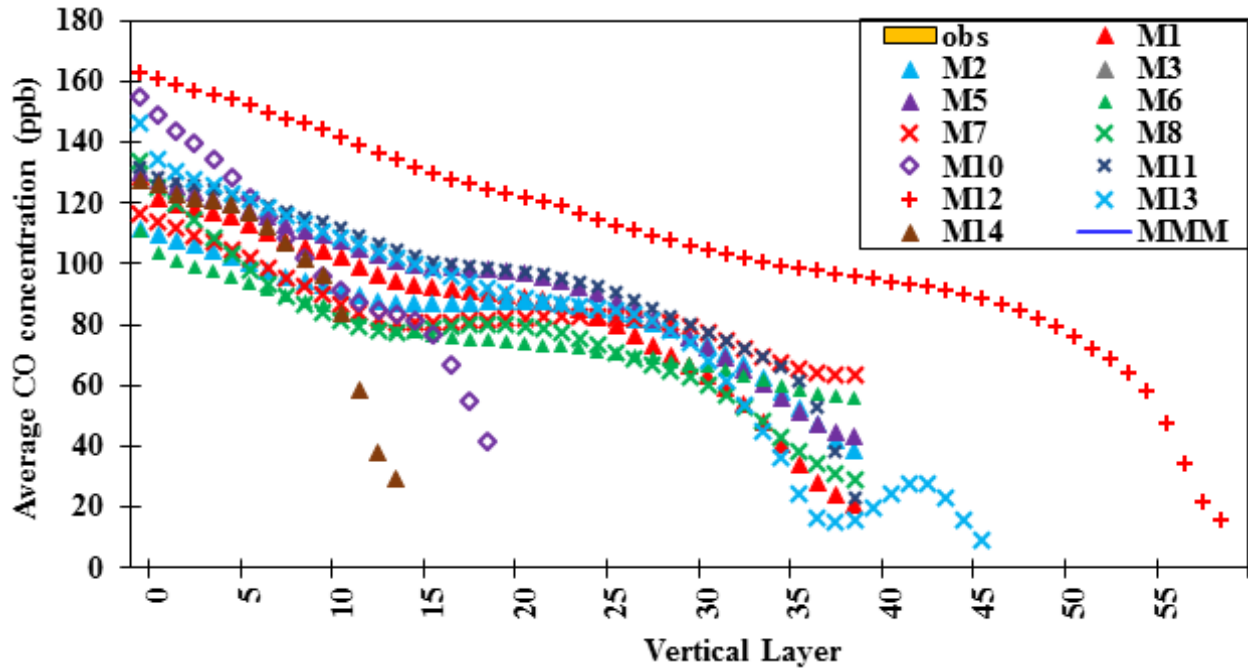


Figure S10 Domain average CO concentrations of models at vertical layers (unit: ppb). Values are calculated by annual average data.

Figure S11

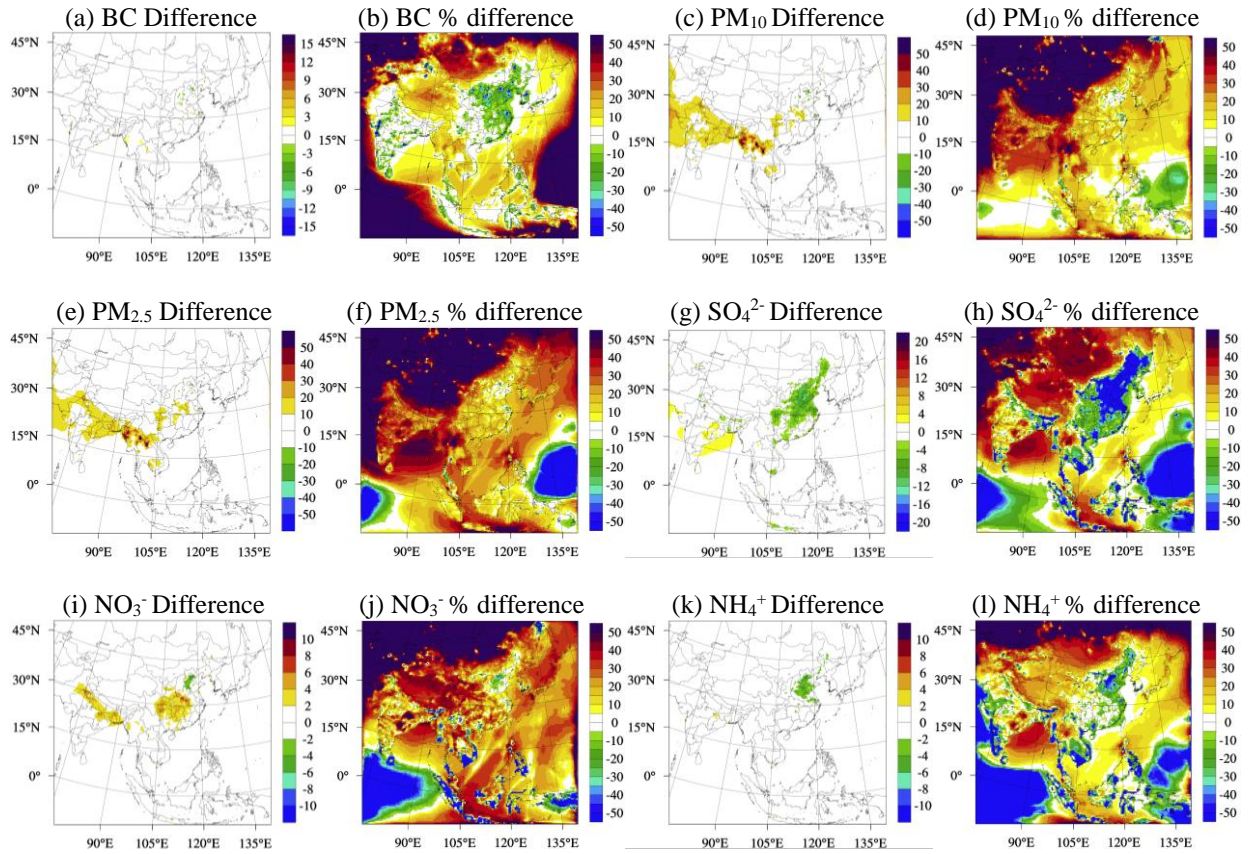


Figure S11 Differences between M1 and M2 at surface layer for (a-b) BC, (c-d) PM₁₀, (e-f) PM_{2.5}, (g-h) SO₄²⁻ (i-j) NO₃⁻ (k-l) NH₄⁺. Values are calculated by annual average data. The difference is calculated by (M1-M2) and % difference is calculated by (M1-M2)/M1×100%. M1 uses GEO-Chem as boundary condition and M2 uses default values of CMAQ model.

Figure S12

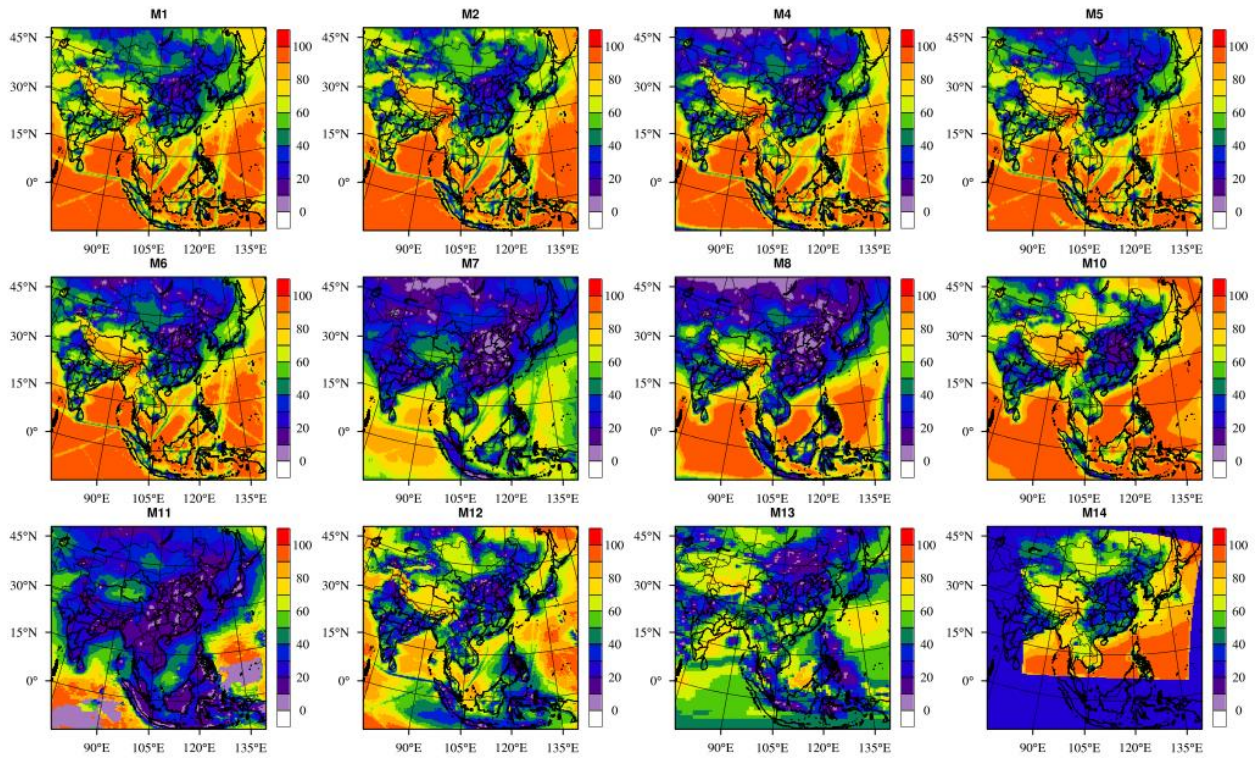


Figure S12 *SOR* values at surface layer for models (unit: %). *SOR* is calculated by $SO_4^{2-}/(SO_2+SO_4^{2-})\times 100\%$. The SO_2 and SO_4^{2-} concentrations are transferred from ppb and $\mu g\ m^{-3}$ to mole(S) m^{-3} before calculating *SOR*. Values are calculated by annual average data.

Figure S13

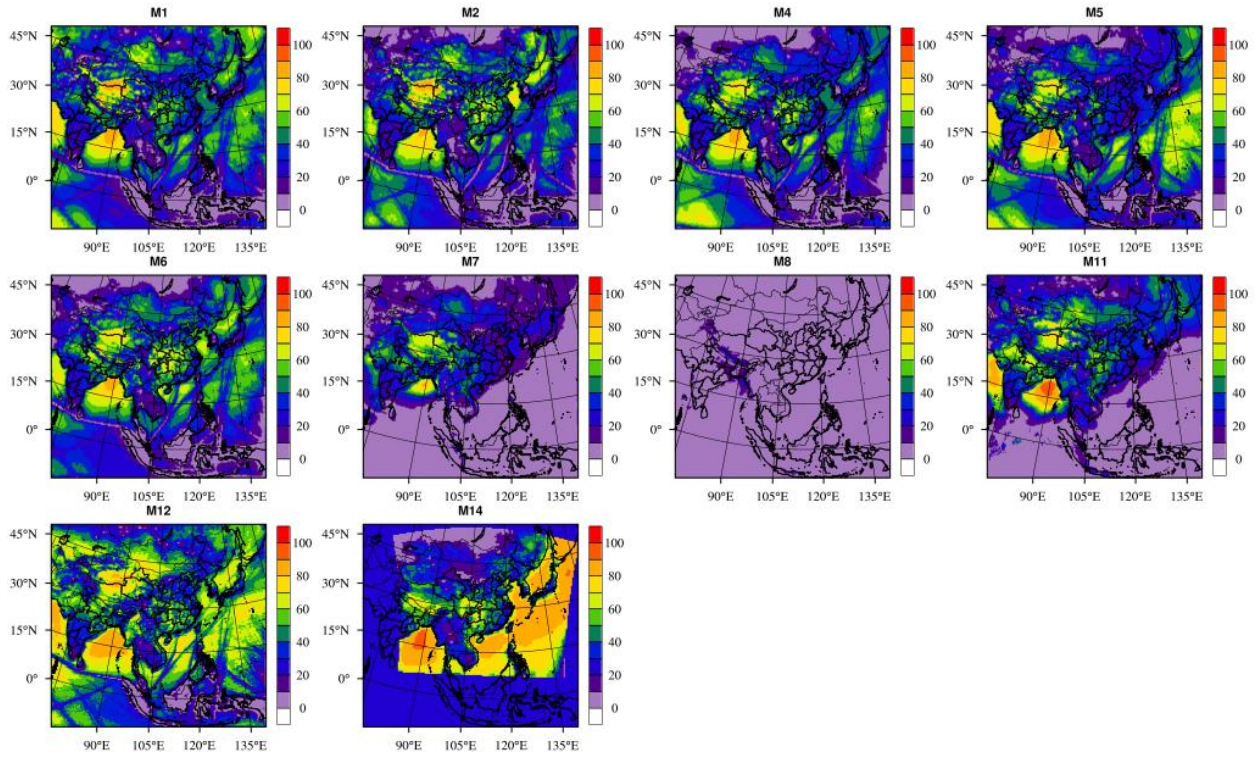
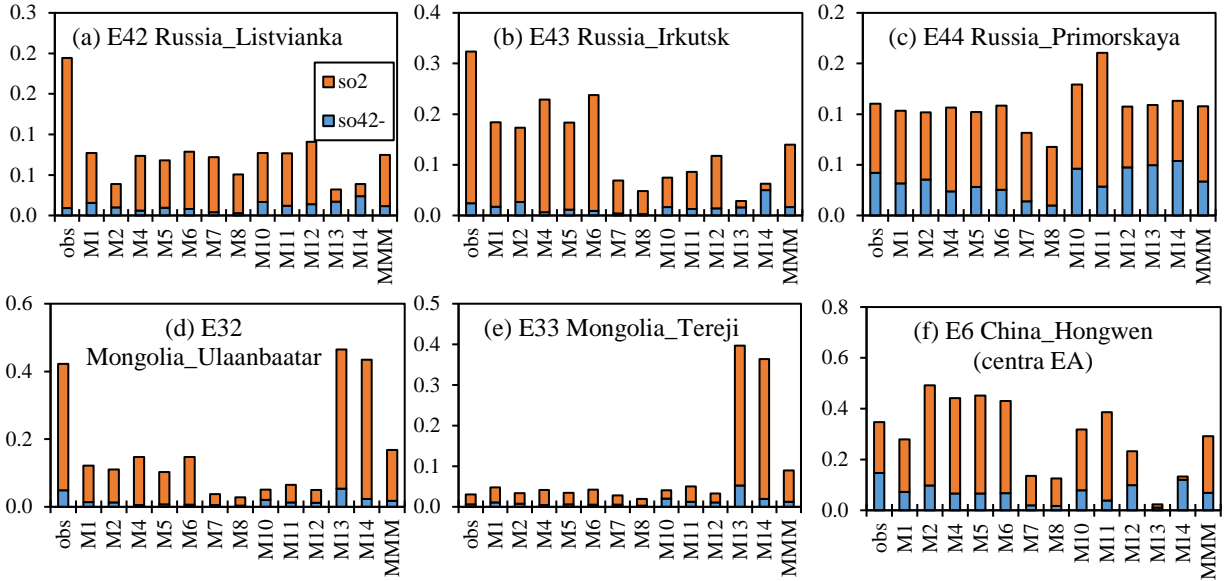


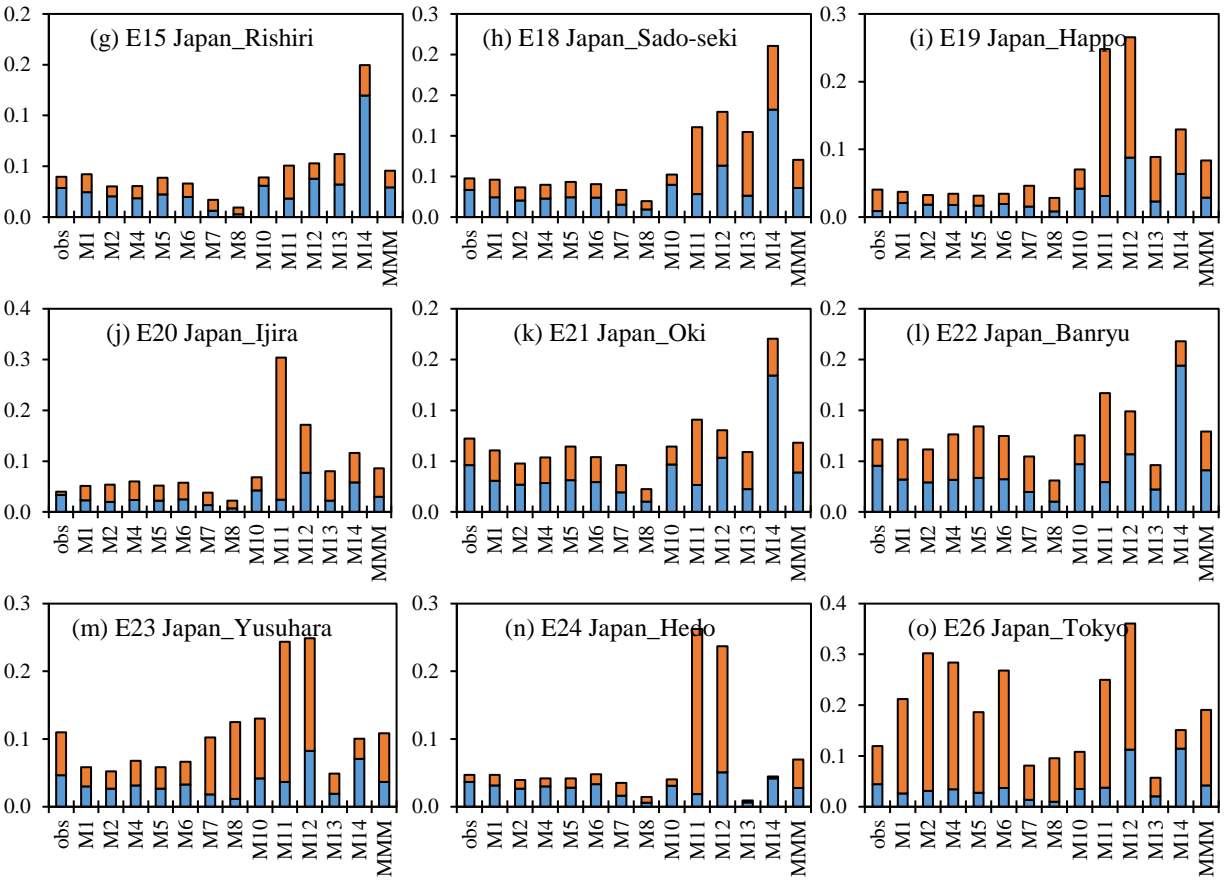
Figure S13 Same as fig S12 but for $C(NO_2)$ (unit: %). $C(NO_2)$ is calculated by $NO_3^- / (NO_2 + NO_3^-) \times 100\%$. The $C(NO_2)$ of M8 is extremely low due to unreasonable low NO_3^- concentration, which is considered as outlier in this study. Values are calculated by annual average data.

Figure S14

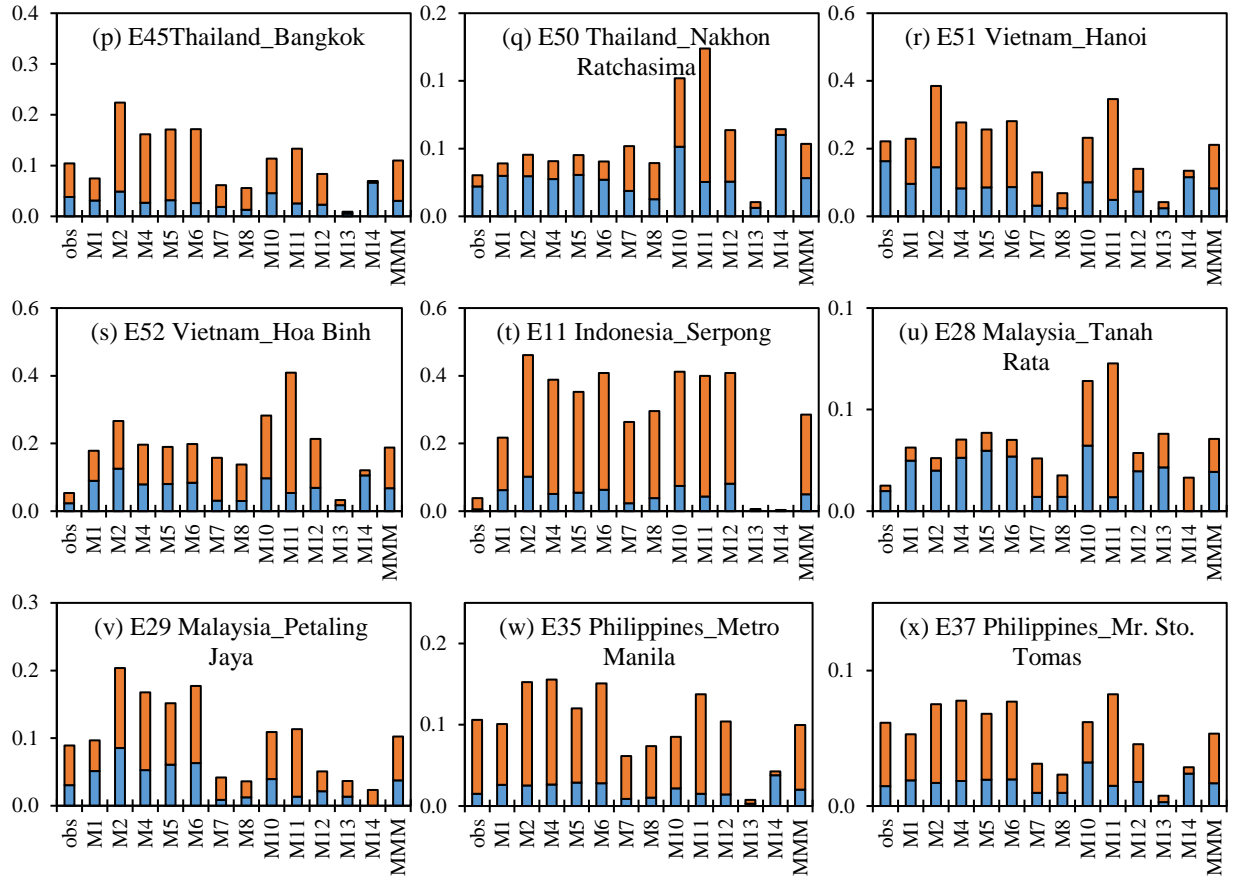
Gas-aerosol partitioning of S in northern EA and central EA



Gas-aerosol partitioning of S in eastern EA



Gas-aerosol partitioning of S in southern EA



Gas-aerosol partitioning of N

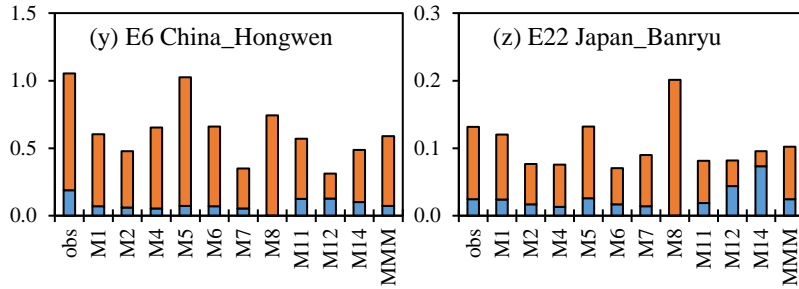


Figure S14 Gas-particle conversion of S and N from observation and individual models at EANET sites. The unit is $\mu\text{mole (S or N) m}^{-3}$. Values are calculated by annual average data.

Figure S15

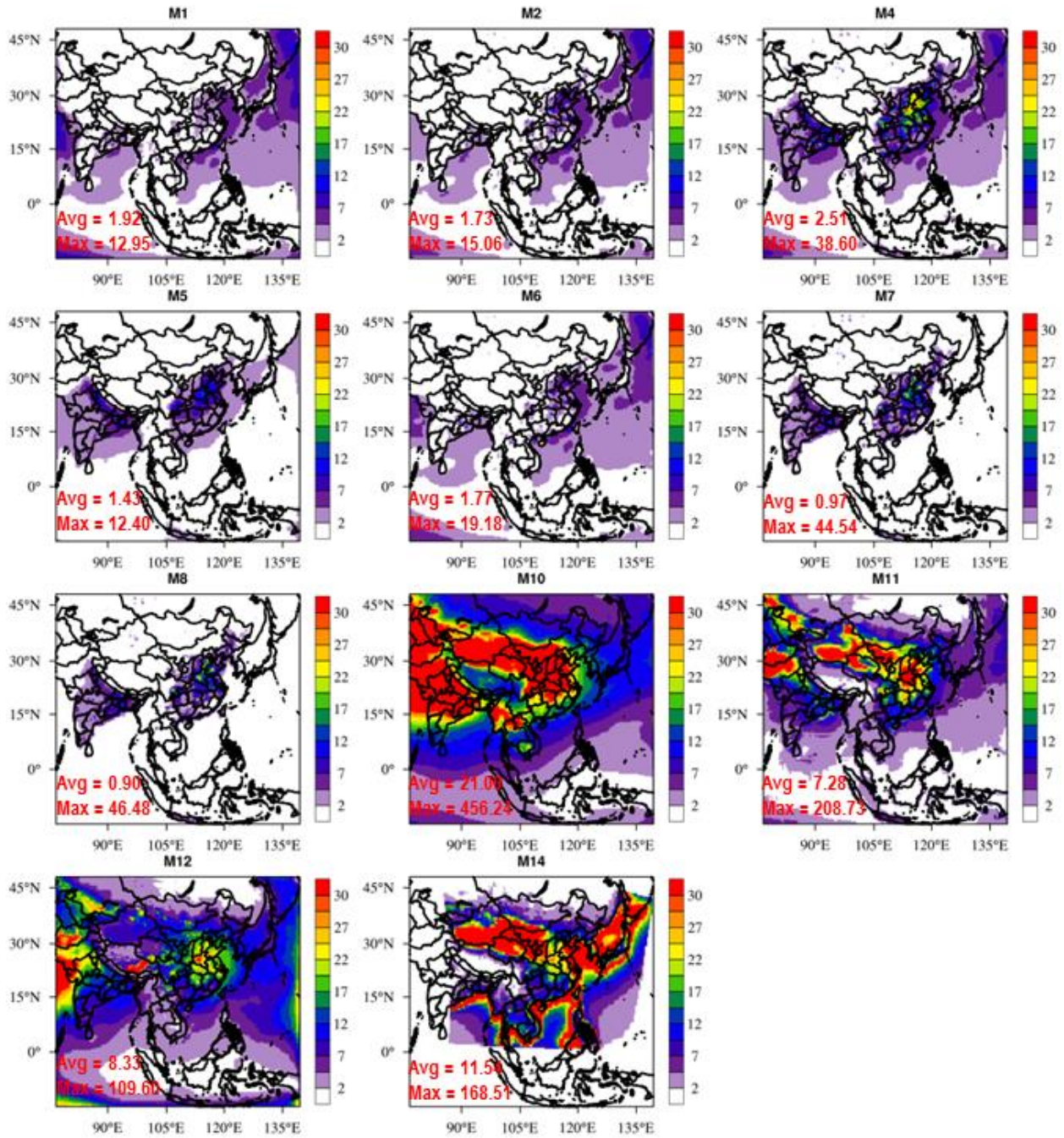


Figure S15 Annual average PMC concentrations at surface layer of individual models ($\mu\text{g m}^{-3}$). The value is calculated by subtracting $\text{PM}_{2.5}$ from PM_{10} . The values in left-bottom are domain average (Avg) and maximum (Max) values.

Table S1Table S1 Multi-model performances on wet deposition (unit: mg(S or N) m⁻² y⁻¹)

	Wet SO ₄ ²⁻ Deposition						Wet NO ₃ ⁻ Deposition					
	M2	M4	M6	M11	M12	MMM	M2	M4	M6	M11	M12	MMM
Mean Obs	931.3	931.3	931.3	931.3	931.3	931.3	460.9	460.9	460.9	460.9	460.9	460.9
Mean MMM	633.7	724.2	775	1313.2	826.2	854.5	187.5	266.7	279.5	597.8	308.3	328
S	0.3	0.3	0.3	0.3	0.2	0.3	0.1	0.1	0.1	0.2	0.1	0.1
MB	-297.7	-207.1	-156.3	381.9	-105.1	-76.9	-273.4	-194.2	-181.4	137	-152.6	-132.9
R	0.5	0.4	0.4	0.2	0.3	0.4	0.1	0.2	0.2	0.2	0.1	0.2
F	61.2	61.2	61.2	24.5	40.8	51	38.8	49	46.9	44.9	38.8	46.9
NMB	-32	-22.2	-16.8	41	-11.3	-8.3	-59.3	-42.1	-39.4	29.7	-33.1	-28.8
NME	49.3	50.2	51.5	117.3	62.8	53.6	66.2	60.9	60.6	78.4	68.8	58.2
MFB	-37.4	-23.4	-15.8	4.6	-11.4	-4.6	-75.8	-49.8	-42.1	25.8	-40.9	-27.6
MFE	57.8	55.9	53.7	93.8	66.7	57.6	84.9	71.2	69.3	61	74.6	62.3
Number of Sites	49	49	49	49	49	49	49	49	49	49	49	49

Continue Table S1

	Wet NH ₄ ⁺ Deposition					
	M2	M4	M6	M11	M12	MMM
Mean Obs	558.4	558.4	558.4	558.4	558.4	558.4
Mean MMM	459.9	349.4	497.4	505	478	337.6
S	0.3	0.1	0.3	0.3	0.2	0.2
MB	-98.5	-208.9	-61	-53.4	-80.4	-220.7
R	0.3	0.2	0.3	0.4	0.4	0.3
F	40.8	44.9	44.9	51	46.9	38.8
NMB	-17.6	-37.4	-10.9	-9.6	-14.4	-39.5
NME	64.8	65.5	64.9	58.2	57	63.6
MFB	-21.2	-42.4	-14.4	-18	-12.6	-41.9
MFE	70.7	77.9	69.1	65.9	62.9	76.1
Number of sites	49	49	49	49	49	49

References:

- Ackermann, I. J., Hass, H., Memmesheimer, M., Ebel, A., Binkowski, F. S., and Shankar, U.: Modal aerosol dynamics model for Europe: Development and first applications, *Atmospheric Environment*, 32, 2981-2999, 1998.
- Appel, K. W., Pouliot, G. A., Simon, H., Sarwar, G., Pye, H. O. T., Napelenok, S. L., Akhtar, F., and Roselle, S. J.: Evaluation of dust and trace metal estimates from the Community Multiscale Air Quality (CMAQ) model version 5.0, *Geoscientific Model Development*, 6, 883-899, 10.5194/gmd-6-883-2013, 2013.
- Carmichael, G. R., Sakurai, T., Streets, D., Hozumi, Y., Ueda, H., Park, S. U., Fung, C., Han, Z., Kajino, M., Engardt, M., Bennet, C., Hayami, H., Sartelet, K., Holloway, T., Wang, Z., Kannari, A., Fu, J., Matsuda, K., Thongboonchoo, N., and Amann, M.: MICS-Asia II: The model intercomparison study for Asia Phase II methodology and overview of findings, *Atmospheric Environment*, 42, 3468-3490, <http://dx.doi.org/10.1016/j.atmosenv.2007.04.007>, 2008.
- Carter: Implementation of the SAPRC-99 Chemical Mechanism into the Models-3 Framework, Report to the United States Environmental Protection Agency, January 29. Available at <http://www.cert.ucr.edu/~carter/absts.htm#s99mod3>). 2000.
- Chen, Z. H., Cheng, S. Y., Li, J. B., Guo, X. R., Wang, W. H., and Chen, D. S.: Relationship between atmospheric pollution processes and synoptic pressure patterns in northern China, *Atmospheric Environment*, 42, 6078-6087, 10.1016/j.atmosenv.2008.03.043, 2008.
- Chin, M., Ginoux, P., Kinne, S., Torres, O., Holben, B. N., Duncan, B. N., Martin, R. V., Logan, J. A., Higurashi, A., and Nakajima, T.: Tropospheric aerosol optical thickness from the GOCART model and comparisons with satellite and Sun photometer measurements, *Journal of the Atmospheric Sciences*, 59, 461-483, 2002.
- Clarke, A. D., Owens, S. R., and Zhou, J. C.: An ultrafine sea-salt flux from breaking waves: Implications for cloud condensation nuclei in the remote marine atmosphere, *J Geophys Res-Atmos*, 111, 2006.
- de Leeuw, G., Neele, F. P., Hill, M., Smith, M. H., and Vignali, E.: Production of sea spray aerosol in the surf zone, *J Geophys Res-Atmos*, 105, 29397-29409, 2000.
- Deng, J. J., Wang, T. J., Jiang, Z. Q., Xie, M., Zhang, R. J., Huang, X. X., and Zhu, J. L.: Characterization of visibility and its affecting factors over Nanjing, China, *Atmospheric Research*, 101, 681-691, 10.1016/j.atmosres.2011.04.016, 2011.
- Foroutan, H., Young, J., Napelenok, S., Ran, L., Appel, K. W., Gilliam, R. C., and Pleim, J. E.: Development and evaluation of a physics-based windblown dust emission scheme implemented in the CMAQ modeling system, *Journal of Advances in Modeling Earth Systems*, 9, 585-608, 10.1002/2016ms000823, 2017.
- Fountoukis, C., and Nenes, A.: ISORROPIA II: a computationally efficient thermodynamic equilibrium model for K^+ - Ca^{2+} - Mg^{2+} - NH_4^+ - Na^+ - SO_4^{2-} - NO_3^- - Cl^- - H_2O aerosols, *Atmospheric Chemistry and Physics*, 7, 4639-4659, 2007.
- Ge, C., Zhang, M. G., Han, Z. W., and Liu, Y. J.: Episode Simulation of Asian Dust Storms with an Air Quality Modeling System, *Advances in Atmospheric Sciences*, 28, 511-520, 2011.
- Gillette, D. A., and Passi, R.: Modeling Dust Emission Caused by Wind Erosion, *J Geophys Res-Atmos*, 93, 14233-14242, 1988.
- Ginoux, P., Chin, M., Tegen, I., Prospero, J. M., Holben, B., Dubovik, O., and Lin, S. J.: Sources and distributions of dust aerosols simulated with the GOCART model, *J Geophys Res-Atmos*, 106, 20255-20273, 2001.
- Gong, S. L.: A parameterization of sea-salt aerosol source function for sub- and super-micron particles, *Global Biogeochem Cy*, 17, 2003.
- Han, Z. W., Ueda, H., Matsuda, K., Zhang, R. J., Arao, K., Kanai, Y., and Hasome, H.: Model study on particle size segregation and deposition during Asian dust events in March 2002, *J Geophys Res-Atmos*, 109, 2004.
- Hao, W. M., Petkov, A., Nordgren, B. L., Corley, R. E., Silverstein, R. P., Urbanski, S. P., Evangelidou, N., Balkanski, Y., and Kinder, B. L.: Daily black carbon emissions from fires in northern Eurasia for 2002-2015, *Geoscientific Model Development*, 9, 4461-4474, 2016.
- Huang, J., Minnis, P., Chen, B., Huang, Z. W., Liu, Z. Y., Zhao, Q. Y., Yi, Y. H., and Ayers, J. K.: Long-range transport and vertical structure of Asian dust from CALIPSO and surface measurements during PACDEX, *J Geophys Res-Atmos*, 113, 10.1029/2008jd010620, 2008.
- Huang, K.: Identification of Missing Anthropogenic Emission Sources in Russia: Implication for Modeling Arctic Haze, *Aerosol Air Qual Res*, 10.4209/aaqr.2014.08.0165, 2014.

- Huang, K., Fu, J. S., Prikhodko, V. Y., Storey, J. M., Romanov, A., Hodson, E. L., Cresko, J., Morozova, I., Ignatieva, Y., and Cabaniss, J.: Russian anthropogenic black carbon: Emission reconstruction and Arctic black carbon simulation, *J Geophys Res-Atmos*, 120, 11306-11333, 2015.
- Im, U.: Impact of sea-salt emissions on the model performance and aerosol chemical composition and deposition in the East Mediterranean coastal regions, *Atmospheric Environment*, 75, 329-340, 2013.
- Iwasaka, Y., Shi, G. Y., Yamada, M., Matsuki, A., Trochkin, D., Kim, Y. S., Zhang, D., Nagatani, T., Shibata, T., Nagatani, M., Nakata, H., Shen, Z., Li, G., and Chen, B.: Importance of dust particles in the free troposphere over the Taklamakan Desert: Electron microscopic experiments of particles collected with a balloonborne particle impactor at Dunhuang, China, *J Geophys Res-Atmos*, 108, 1-10, 10.1029/2002jd003270, 2003.
- Kelly, J. T., Bhave, P. V., Nolte, C. G., Shankar, U., and Foley, K. M.: Simulating emission and chemical evolution of coarse sea-salt particles in the Community Multiscale Air Quality (CMAQ) model, *Geoscientific Model Development*, 3, 257-273, 2010.
- Kholod, N., Evans, M., and Kuklinski, T.: Russia's black carbon emissions: focus on diesel sources, *Atmospheric Chemistry and Physics*, 16, 2016.
- Li, J. Y., Zhang, H. L., and Ying, Q.: Comparison of the SAPRC07 and SAPRC99 photochemical mechanisms during a high ozone episode in Texas: Differences in concentrations, OH budget and relative response factors, *Atmospheric Environment*, 54, 25-35, 10.1016/j.atmosenv.2012.02.034, 2012.
- Li, M., Zhang, Q., Kurokawa, J. I., Woo, J. H., He, K., Lu, Z., Ohara, T., Song, Y., Streets, D. G., Carmichael, G. R., Cheng, Y., Hong, C., Huo, H., Jiang, X., Kang, S., Liu, F., Su, H., and Zheng, B.: MIX: a mosaic Asian anthropogenic emission inventory under the international collaboration framework of the MICS-Asia and HTAP, *Atmos. Chem. Phys.*, 17, 935-963, 10.5194/acp-17-935-2017, 2017.
- Liu, M., Westphal, D. L., Wang, S. G., Shimizu, A., Sugimoto, N., Zhou, J., and Chen, Y.: A high-resolution numerical study of the Asian dust storms of April 2001, *J Geophys Res-Atmos*, 108, 10.1029/2002jd003178, 2003.
- Liu, Y. M., Zhang, S. T., Fan, Q., Wu, D., Chan, P. W., Wang, X. M., Fan, S. J., Feng, Y. R., and Hong, Y. Y.: Accessing the Impact of Sea-Salt Emissions on Aerosol Chemical Formation and Deposition over Pearl River Delta, China, *Aerosol Air Qual Res*, 15, 2232-2245, 2015.
- Murphy, B. N., and Pandis, S. N.: Simulating the Formation of Semivolatile Primary and Secondary Organic Aerosol in a Regional Chemical Transport Model, *Environmental science & technology*, 43, 4722-4728, 2009.
- Nenes, A., Pandis, S. N., and Pilinis, C.: ISORROPIA: A new thermodynamic equilibrium model for multiphase multicomponent inorganic aerosols, *Aquat Geochem*, 4, 123-152, 1998.
- Nenes, A., Pandis, S. N., and Pilinis, C.: Continued development and testing of a new thermodynamic aerosol module for urban and regional air quality models, *Atmospheric Environment*, 33, 1553-1560, 1999.
- Neumann, D., Matthias, V., Bieser, J., Aulinger, A., and Quante, M.: A comparison of sea salt emission parameterizations in northwestern Europe using a chemistry transport model setup, *Atmospheric Chemistry and Physics*, 16, 9905-9933, 2016.
- Qu, W. J., Arimoto, R., Zhang, X. Y., Zhao, C. H., Wang, Y. Q., Sheng, L. F., and Fu, G.: Spatial distribution and interannual variation of surface PM10 concentrations over eighty-six Chinese cities, *Atmospheric Chemistry and Physics*, 10, 5641-5662, 10.5194/acp-10-5641-2010, 2010.
- Sartelet, K. N., Hayami, H., and Sportisse, B.: MICS Asia Phase II—Sensitivity to the aerosol module, *Atmospheric Environment*, 42, 3562-3570, <http://dx.doi.org/10.1016/j.atmosenv.2007.03.005>, 2008.
- Shao, Y. P., Wyrwoll, K. H., Chappell, A., Huang, J. P., Lin, Z. H., McTainsh, G. H., Mikami, M., Tanaka, T. Y., Wang, X. L., and Yoon, S.: Dust cycle: An emerging core theme in Earth system science, *Aeolian Res*, 2, 181-204, 2011.
- Shearer, S. M., Harley, R. A., Jin, L., and Brown, N. J.: Comparison of SAPRC99 and SAPRC07 mechanisms in photochemical modeling for central California, *Atmospheric Environment*, 46, 205-216, 10.1016/j.atmosenv.2011.09.079, 2012.
- Stockwell, W. R., Middleton, P., Chang, J. S., and Tang, X. Y.: The 2nd Generation Regional Acid Deposition Model Chemical Mechanism for Regional Air-Quality Modeling, *J Geophys Res-Atmos*, 95, 16343-16367, 1990.
- Stockwell, W. R., Kirchner, F., Kuhn, M., and Seefeld, S.: A new mechanism for regional atmospheric chemistry modeling, *J Geophys Res-Atmos*, 102, 25847-25879, 1997.
- Wang, K., Zhang, Y., Nenes, A., and Fountoukis, C.: Implementation of dust emission and chemistry into the Community Multiscale Air Quality modeling system and initial application to an Asian dust storm episode, *Atmospheric Chemistry and Physics*, 12, 10209-10237, 2012a.

- Wang, T. J., Jiang, F., Deng, J. J., Shen, Y., Fu, Q. Y., Wang, Q., Fu, Y., Xu, J. H., and Zhang, D. N.: Urban air quality and regional haze weather forecast for Yangtze River Delta region, *Atmospheric Environment*, 58, 70-83, 10.1016/j.atmosenv.2012.01.014, 2012b.
- Wang, Z., Pan, X. L., Uno, I., Li, J., Wang, Z. F., Chen, X. S., Fu, P. Q., Yang, T., Kobayashi, H., Shimizu, A., Sugimoto, N., and Yamamoto, S.: Significant impacts of heterogeneous reactions on the chemical composition and mixing state of dust particles: A case study during dust events over northern China, *Atmospheric Environment*, 159, 83-91, 2017.
- Wang, Z., Pan, X. L., Uno, I., Chen, X. S., Yamamoto, S., Zheng, H. T., Li, J., and Wang, Z. F.: Importance of mineral dust and anthropogenic pollutants mixing during a long-lasting high PM event over East Asia, *Environ Pollut*, 234, 368-378, 2018.
- Webb, N. P., and Pierre, C.: Quantifying Anthropogenic Dust Emissions, *Earths Future*, 6, 286-295, 2018.
- Wesely, M. L.: Parameterization of Surface Resistances to Gaseous Dry Deposition in Regional-Scale Numerical-Models, *Atmospheric Environment*, 23, 1293-1304, 1989.
- Xing, J., Mathur, R., Pleim, J., Hogrefe, C., Gan, C. M., Wong, D. C., Wei, C., Gilliam, R., and Pouliot, G.: Observations and modeling of air quality trends over 1990-2010 across the Northern Hemisphere: China, the United States and Europe, *Atmospheric Chemistry and Physics*, 15, 2723-2747, 10.5194/acp-15-2723-2015, 2015.
- Zaveri, R. A., and Peters, L. K.: A new lumped structure photochemical mechanism for large-scale applications, *J Geophys Res-Atmos*, 104, 30387-30415, 1999.
- Zhang, L., Brook, J. R., and Vet, R.: A revised parameterization for gaseous dry deposition in air-quality models, *Atmospheric Chemistry and Physics*, 3, 2067-2082, 2003.
- Zheng, B., Zhang, Q., Zhang, Y., He, K. B., Wang, K., Zheng, G. J., Duan, F. K., Ma, Y. L., and Kimoto, T.: Heterogeneous chemistry: a mechanism missing in current models to explain secondary inorganic aerosol formation during the January 2013 haze episode in North China, *Atmospheric Chemistry and Physics*, 15, 2031-2049, 2015.